CrossMark

The PHANGS–JWST Treasury Survey: Star Formation, Feedback, and Dust Physics at High Angular Resolution in Nearby GalaxieS

Janice C. Lee[1,2], Karin M. Sandstrom[3], Adam K. Leroy[4], David A. Thilker[5], Eva Schinnerer[6], Erik Rosolowsky[7],
Kirsten L. Larson[8], Oleg V. Egorov[9,10], Thomas G. Williams[6], Judy Schmidt[11], Eric Emsellem[12,13],
Gagandeep S. Anand[14], Ashley T. Barnes[15], Francesco Belfiore[16], Ivana Bešlić[17], Frank Bigiel[15],
Guillermo A. Blanc[18,19], Alberto D. Bolatto[20], Médéric Boquien[21], Jakob den Brok[22], Yixian Cao[23],
Rupali Chandar[24], Jérémy Chastenet[25], Mélanie Chevance[26,27], I-Da Chiang (江宜達)[28], Enrico Congiu[19],
Daniel A. Dale[29], Sinan Deger[30,31], Cosima Eibensteiner[32], Christopher M. Faesi[33], Simon C. O. Glover[26],
Kathryn Grasha[34], Brent Groves[34,35], Hamid Hassani[7], Kiana F. Henny[29], Jonathan D. Henshaw[6,36],
Nils Hoyer[6,37,38], Annie Hughes[39,40], Sarah Jeffreson[41], María J. Jiménez-Donaire[42,43], Jaeyeon Kim[26],
Hwihyun Kim[44], Ralf S. Klessen[26,45], Eric W. Koch[41], Kathryn Kreckel[9], J. M. Diederik Kruijssen[27], Jing Li[46],
Daizhong Liu[47], Laura A. Lopez[4,48,49], Daniel Maschmann[2,50], Ness Mayker Chen[4,48], Sharon E. Meidt[25],
Eric J. Murphy[51], Justus Neumann[6], Nadine Neumayer[6], Hsi-An Pan[52], Ismael Pessa[6,53], Jérôme Pety[54,55],
Miguel Querejeta[42], Francesca Pinna[6], M. Jimena Rodríguez[2,56], Toshiki Saito[57], Patricia Sánchez-Blázquez[58,59],
Francesco Santoro[6], Amy Sardone[4,48], Rowan J. Smith[60], Mattia C. Sormani[26], Fabian Scheuermann[9],
Sophia K. Stuber[6], Jessica Sutter[61], Jiayi Sun (孙嘉懿)[62,63], Yu-Hsuan Teng[3], Robin G. Treß[64], Antonio Usero[42],
Elizabeth J. Watkins[9], Bradley C. Whitmore[14], and Alessandro Razza[19]

[1] Gemini Observatory/NSF's NOIRLab, 950 North Cherry Avenue, Tucson, AZ, 85719, USA; janice.lee@noirlab.edu
[2] Steward Observatory, University of Arizona, 933 North Cherry Avenue, Tucson, AZ 85721, USA
[3] Center for Astrophysics and Space Sciences, Department of Physics, University of California, San Diego, 9500 Gilman Drive, La Jolla, CA 92093, USA
[4] Department of Astronomy, The Ohio State University, 140 West 18th Avenue, Columbus, OH 43210, USA
[5] Department of Physics and Astronomy, The Johns Hopkins University, Baltimore, MD 21218, USA
[6] Max-Planck-Institut für Astronomie, Königstuhl 17, D-69117, Heidelberg, Germany
[7] Department of Physics, University of Alberta, Edmonton, AB T6G 2E1, Canada
[8] AURA for the European Space Agency (ESA), Space Telescope Science Institute, 3700 San Martin Drive, Baltimore, MD 21218, USA
[9] Astronomisches Rechen-Institut, Zentrum für Astronomie der Universität Heidelberg, Mönchhofstraße 12-14, D-69120 Heidelberg, Germany
[10] Sternberg Astronomical Institute, Lomonosov Moscow State University, Universitetsky pr. 13, 119234 Moscow, Russia
[11] Astrophysics Source Code Library, Michigan Technological University, 1400 Townsend Drive, Houghton, MI 49931, USA
[12] European Southern Observatory, Karl-Schwarzschild Straße 2, D-85748 Garching bei München, Germany
[13] Univ Lyon, Univ Lyon 1, ENS de Lyon, CNRS, Centre de Recherche Astrophysique de Lyon UMR5574, F-69230 Saint-Genis-Laval, France
[14] Space Telescope Science Institute, 3700 San Martin Drive, Baltimore, MD 21218, USA
[15] Argelander-Institut für Astronomie, Universität Bonn, Auf dem Hügel 71, D-53121 Bonn, Germany
[16] INAF—Osservatorio Astrofisico di Arcetri, Largo E. Fermi 5, I-50157, Firenze, Italy
[17] Argelander-Institut für Astronomie, Universität Bonn, Auf dem Hügel 71, D-53121 Bonn, Germany
[18] Observatories of the Carnegie Institution for Science, 813 Santa Barbara Street, Pasadena, CA 91101, USA
[19] Departamento de Astronomía, Universidad de Chile, Camino del Observatorio 1515, Las Condes, Santiago, Chile
[20] Department of Astronomy and Joint Space-Science Institute, University of Maryland, College Park, MD 20742, USA
[21] Centro de Astronomía (CITEVA), Universidad de Antofagasta, Avenida Angamos 601, Antofagasta, Chile
[22] Argelander-Institut für Astronomie, Universität Bonn, Auf dem Hügel 71, D-53121 Bonn, Germany
[23] Max-Planck-Institut für Extraterrestrische Physik (MPE), Giessenbachstr. 1, D-85748 Garching, Germany
[24] University of Toledo, 2801 West Bancroft Street, Mail Stop 111, Toledo, OH 43606, USA
[25] Sterrenkundig Observatorium, Universiteit Gent, Krijgslaan 281 S9, B-9000 Gent, Belgium
[26] Universität Heidelberg, Zentrum für Astronomie, Institut für Theoretische Astrophysik, Albert-Ueberle-Str 2, D-69120 Heidelberg, Germany
[27] Cosmic Origins Of Life (COOL) Research DAO, coolresearch.io
[28] Institute of Astronomy and Astrophysics, Academia Sinica, No. 1, Sec. 4, Roosevelt Road, Taipei 10617, Taiwan
[29] Department of Physics and Astronomy, University of Wyoming, Laramie, WY 82071, USA
[30] California Institute of Technology, 1200 East California Boulevard, MC 249-17, Pasadena, CA 91125, USA
[31] The Oskar Klein Centre for Cosmoparticle Physics, Department of Physics, Stockholm University, AlbaNova, Stockholm, SE-106 91, Sweden
[32] Argelander-Institut für Astronomie, Universität Bonn, Auf dem Hügel 71, 53121 Bonn, Germany
[33] University of Connecticut, Department of Physics, 196A Auditorium Road, Unit 3046, Storrs, CT 06269, USA
[34] Research School of Astronomy and Astrophysics, Australian National University, Canberra, ACT 2611, Australia
[35] International Centre for Radio Astronomy Research, University of Western Australia, 35 Stirling Highway, Crawley, WA 6009, Australia
[36] Astrophysics Research Institute, Liverpool John Moores University, 146 Brownlow Hill, Liverpool L3 5RF, UK
[37] Donostia International Physics Center, Paseo Manuel de Lardizabal 4, E-20118 Donostia-San Sebastián, Spain
[38] Universität Heidelberg, Seminarstrasse 2, D-69117 Heidelberg, Germany
[39] CNRS, IRAP, 9 Av. du Colonel Roche, BP 44346, F-31028 Toulouse cedex 4, France
[40] Université de Toulouse, UPS-OMP, IRAP, F-31028 Toulouse cedex 4, France
[41] Center for Astrophysics |Harvard & Smithsonian, 60 Garden Street, Cambridge, MA 02138, USA
[42] Observatorio Astronómico Nacional (IGN), C/Alfonso XII, 3, E-28014 Madrid, Spain
[43] Centro de Desarrollos Tecnológicos, Observatorio de Yebes (IGN), 19141 Yebes, Guadalajara, Spain
[44] Gemini Observatory/NSF's NOIRLab, 950 North Cherry Avenue, Tucson, AZ, USA
[45] Universität Heidelberg, Interdisziplinäres Zentrum für Wissenschaftliches Rechnen, Im Neuenheimer Feld 205, D-69120 Heidelberg, Germany
[46] Astronomisches Rechen-Institut, Zentrum für Astronomie der Universität Heidelberg, Mönchhofstraße 12-14, D-69120 Heidelberg, Germany
[47] Max-Planck-Institut für extraterrestrische Physik, Giessenbachstraße 1, D-85748 Garching, Germany
[48] Center for Cosmology and Astroparticle Physics, 191 West Woodruff Avenue, Columbus, OH 43210, USA
[49] Flatiron Institute, Center for Computational Astrophysics, New York, NY 10010, USA
[50] Sorbonne Université, LERMA, Observatoire de Paris, PSL University, CNRS, F-75014, Paris, France

[51] National Radio Astronomy Observatory, 520 Edgemont Road, Charlottesville, VA 22903, USA

[52] Department of Physics, Tamkang University, No. 151, Yingzhuan Road, Tamsui District, New Taipei City 251301, Taiwan

[53] Leibniz-Institut für Astrophysik Potsdam (AIP), An der Sternwarte 16, D-14482 Potsdam, Germany

[54] Institut de Radioastronomie Millimétrique (IRAM), 300 Rue de la Piscine, F-38406 Saint Martin d'Hères, France

[55] Observatoire de Paris, PSL Research University, CNRS, Sorbonne Universités, F-75014 Paris, France

[56] Instituto de Astrofísica de La Plata, CONICET–UNLP, Paseo del Bosque S/N, B1900FWA La Plata, Argentina

[57] National Astronomical Observatory of Japan, 2-21-1 Osawa, Mitaka, Tokyo, 181-8588, Japan

[58] Departamento de Física de la Tierra y Astrofísica, Universidad Complutense de Madrid, E-28040 Madrid, Spain

[59] Instituto de Física de Partículas y del Cosmos, Universidad Complutense de Madrid, E-28040 Madrid, Spain

[60] Jodrell Bank Center for Astrophysics, Department of Physics and Astronomy, University of Manchester, Oxford Road, Manchester M13 9PL, UK

[61] Center for Astrophysics & Space Sciences, Department of Physics, University of California, San Diego, 9500 Gilman Drive, San Diego, CA 92093, USA

[62] Department of Physics and Astronomy, McMaster University, 1280 Main Street West, Hamilton, ON L8S 4M1, Canada

[63] Canadian Institute for Theoretical Astrophysics (CITA), University of Toronto, 60 St George Street, Toronto, ON M5S 3H8, Canada

[64] Institute of Physics, Laboratory for Galaxy Evolution and Spectral Modelling, EPFL, Observatoire de Sauverny, Chemin Pegais 51, 1290 Versoix, Switzerland.

Abstract

The PHANGS collaboration has been building a reference data set for the multiscale, multiphase study of star formation and the interstellar medium (ISM) in nearby galaxies. With the successful launch and commissioning of JWST, we can now obtain high-resolution infrared imaging to probe the youngest stellar populations and dust emission on the scales of star clusters and molecular clouds (∼5–50 pc). In Cycle 1, PHANGS is conducting an eight-band imaging survey from 2 to 21 μm of 19 nearby spiral galaxies. Optical integral field spectroscopy, CO(2–1) mapping, and UV-optical imaging for all 19 galaxies have been obtained through large programs with ALMA, VLT-MUSE, and Hubble. PHANGS–JWST enables a full inventory of star formation, accurate measurement of the mass and age of star clusters, identification of the youngest embedded stellar populations, and characterization of the physical state of small dust grains. When combined with Hubble catalogs of ∼10,000 star clusters, MUSE spectroscopic mapping of ∼20,000 H II regions, and ∼12,000 ALMA-identified molecular clouds, it becomes possible to measure the timescales and efficiencies of the earliest phases of star formation and feedback, build an empirical model of the dependence of small dust grain properties on local ISM conditions, and test our understanding of how dust-reprocessed starlight traces star formation activity, all across a diversity of galactic environments. Here we describe the PHANGS–JWST Treasury survey, present the remarkable imaging obtained in the first few months of science operations, and provide context for the initial results presented in the first series of PHANGS–JWST publications.

1. Introduction

The discovery of infrared emission in the Orion Nebula revealed that the earliest phases of star formation occur in the densest, dust-enshrouded cores of molecular clouds that are not observable in the optical (Becklin & Neugebauer 1967; Kleinmann & Low 1967). Beginning with IRAS in the 1980s (Neugebauer et al. 1984), a series of cryogenic infrared space missions, including the Infrared Space Observatory, Spitzer, and Herschel (Kessler et al. 2003; Werner et al. 2004; Pilbratt et al. 2010), mapped emission from star formation and dust with increasing resolution and coverage across the mid- and far-infrared (e.g., Soifer et al. 1987, 2008; Kennicutt & Evans 2012, and references therein). These missions demonstrated that infrared observations are a requisite component for understanding the process of star formation in galaxies and the physics of the interstellar medium (ISM). With the transformative infrared capabilities of JWST, studies of star formation and dust in galaxies are again entering a new era. New breakthroughs in this field will rely on JWST as well as the collective effort of the astronomy community to conduct observations

across the electromagnetic spectrum that capture all major stages of the star formation cycle, from gas to stars.

For nearby galaxies, JWST is finally extending the high spatial resolution infrared studies of star formation and dust previously only possible in the Milky Way and Local Group to galaxies within a few tens of megaparsecs. Here we introduce the Physics at High Angular resolution in Nearby GalaxieS (PHANGS)–JWST Cycle 1 Treasury survey, which was designed to use JWST's order-of-magnitude improvement in sensitivity and angular resolution to map infrared emission from the youngest stellar populations and dusty ISM across the disks of galaxies on scales of tens of parsecs. These are the physical scales where gas fragmentation is expected (e.g., due to the Jeans instability) and the key physical processes that drive, regulate, and extinguish star formation can be investigated for individual star clusters (∼5 pc), H II regions (∼10 pc), and molecular clouds (∼50 pc).

Imaging in eight bands from 2 to 21 μm is being obtained for 19 nearby (d < 20 Mpc) spiral galaxies. All have UV-optical imaging from the Hubble Space Telescope (HST; Lee et al. 2022),[65] optical integral field spectroscopy from MUSE on the Very Large Telescope (VLT; Emsellem et al. 2022), and CO(2–1) mapping from the Atacama Large Millimeter/submillimeter Array (ALMA; Leroy et al. 2021) through

---

[65] HST UV-optical imaging available on MAST: doi:10.17909/t9-r08f-dq31.

survey programs led by the PHANGS collaboration (Schinnerer et al. 2019a). All data are publicly available from the respective observatory's archives, and HST catalogs of ≳10,000 star clusters and associations[66] (Whitmore et al. 2021; Deger et al. 2022; Larson et al. 2022; Thilker et al. 2022), MUSE catalogs of ≳20,000 H II regions (Groves et al. 2023; Santoro et al. 2022), and ALMA catalogs of ≳12,000 molecular clouds (Sun et al. 2018, 2022; Rosolowsky et al. 2021) have been produced.[67]

The PHANGS–JWST sample covers the range of star formation, gas, dust, structural, and dynamical properties found in present-day massive galaxies on the star-forming main sequence, enabling studies that connect small-scale gas and star formation physics to the broader context of galactic structure and galaxy evolution. The combined PHANGS multiwavelength observational programs yield the first data set that accesses all key stages of the star formation cycle at the resolution of individual star-forming regions across a sample that reflects the galactic environments where the majority of star formation occurs at $z = 0$ (e.g., Brinchmann et al. 2004; Salim et al. 2007; Saintonge et al. 2017).

PHANGS targets were among the first to be observed after the successful completion of JWST commissioning in 2022 June. Within the first 2 months of science operations, data for four galaxies (NGC 7496, IC 5332, NGC 628, and NGC 1365) were obtained. As a Treasury program, the PHANGS–JWST imaging data have no exclusive access period. The release of the data shortly after observation revealed the architecture of the dusty ISM in exquisite detail, capturing the attention of not only the science community but also of the general public and press.

Analysis by the PHANGS collaboration is underway and focuses on the following science goals.

1. Characterization of the youngest embedded stellar populations that are inaccessible at optical-UV wavelengths, completion of the inventory of newborn stars, and definitive measurement of star cluster mass functions and formation efficiencies to probe the early evolution of stars and star cluster populations.
2. Characterization of ISM bubble and shell features and measurement of the duration of dust-embedded star formation and star formation efficiencies to identify the sources and timescales of star formation feedback.
3. Determination of how local interstellar conditions influence the properties, evolution, and processing of the smallest dust grains, in particular the polycyclic aromatic hydrocarbons (PAHs), to enable a physically robust interpretation of dust emission in nearby galaxies.
4. Development of new dust-based high-resolution tracers of the neutral gas that are complementary to H I, CO, C I, and C^+ mapping to resolve the multiscale filamentary structure of the ISM.
5. Establishment and calibration of robust mid-IR diagnostics of star formation activity that account for the youngest stars to compute star formation rates (SFRs) from cloud to galaxy scales.

This paper is intended to provide a general reference for the parameters of the survey, as well as an introduction for the

papers in this Issue, which showcases some of the science possible based on PHANGS–JWST data for the first four galaxies observed. The remaining sections are organized as follows. In Section 2, we describe the galaxy sample and provide a brief summary of the supporting multiwavelength PHANGS data sets. Our observing strategy with NIRCam and MIRI is presented in Section 3. Next, in Section 4, we describe our early data reduction efforts to enable first science, focusing on modifications made to the standard STScI JWST Science Calibration Pipeline, and note some limitations for the use of these early data. In Section 5, we present the imaging for NGC 7496, IC 5332, NGC 628, and NGC 1365. In Section 6, we describe the scientific goals that motivate the PHANGS–JWST survey and highlight results presented in this Issue. In Section 7, we describe the image products that will be released by the PHANGS team and provide examples of additional JWST high-level science products that would be valuable to develop from the ensemble of panchromatic PHANGS data sets. We conclude with a short summary in Section 7.

2. Galaxy Sample

The PHANGS–JWST Treasury survey targets the 19 PHANGS galaxies that have the full complement of UV-optical imaging from PHANGS–HST[68] (Lee et al. 2022), optical spectral mapping from PHANGS–MUSE (Emsellem et al. 2022), and millimeter-wave spectral mapping from PHANGS–ALMA (Leroy et al. 2021). In addition to these major survey data sets from JWST, HST, VLT-MUSE, and ALMA, a wealth of additional supporting data from the PHANGS collaboration has been and continues to be obtained, e.g., Astrosat far-/near-ultraviolet imaging (PI: E. Rosolowsky), HST Hα narrowband imaging (PI: R. Chandar), ground-based wide-field Hα narrowband imaging (PIs: G. Blanc, I.-T. Ho), and H I 21 cm observations from team programs with the VLA and Meer-KAT. A complete listing of PHANGS observations and data products is provided at www.phangs.org/data.

The basic properties of the galaxies relevant to their selection are given in Tables 1 and 2, and Figure 1 shows MUSE+ALMA composite images for the full sample.

Over the distance range of these galaxies (5–20 Mpc; Table 1), JWST's point-spread function (PSF) FWHM subtends 2–6 pc at 2 μm and 17–65 pc at 21 μm. For the first time, JWST allows for mid-infrared imaging of individual star clusters, H II regions, and molecular clouds across the nearby galaxy population that are well matched to observations of these populations from HST, MUSE, and ALMA. The combination of data sets from these four facilities is essential for achieving our specific science goals (Section 6), and the PHANGS program currently provides the largest uniform collection of such data for galaxies in the local volume.

The PHANGS surveys focus on nearby, star-forming, relatively face-on spiral galaxies. The parent sample ($N = 90$), described in Leroy et al. (2021), aimed to select galaxies visible from the southern hemisphere (i.e., observable by ALMA and the VLT) that have inclinations less that ∼75°, distances less than ∼17 Mpc, stellar masses ≳$5 \times 10^9\ M_\odot$, and specific SFRs, SFR/$M_\star$, above ∼10^{-11} yr^{-1}. The inclination criterion minimizes source blending within the galaxies and line-of-sight dust attenuation. The distance requirement ensures that the galaxies are close enough that HST and JWST can resolve individual clusters and associations, MUSE

Table 1
PHANGS–JWST Target Galaxy Distance, Orientation, and Morphology

Galaxy	α (J2000)	δ (J2000)	D[a] (Mpc)	σ_D[a] (Mpc)	Method[a]	i[b] (deg)	PA[b] (deg)	T[c]	Morphology[c]
NGC 0628[e]	01ʰ36ᵐ41ˢ75	+15ᵈ47ᵐ01ˢ2	9.84	0.63	TRGB[1]	9	21	5.2	SA(s)c
NGC 1087	02ʰ46ᵐ25ˢ16	−00ᵈ29ᵐ55ˢ1	15.85	2.24	Group[2]	43	359	5.2	SB(rs)cdpec
NGC 1300	03ʰ19ᵐ41ˢ08	−19ᵈ24ᵐ40ˢ9	18.99	2.85	NAM[3,4]	32	278	4	(R')SB(s,bl,nrl)b
NGC 1365[e]	03ʰ33ᵐ36ˢ37	−36ᵈ08ᵐ25ˢ4	19.57	0.78	TRGB[1]	55	201	3.2	(R')SB(rs̲,nr)bc
NGC 1385	03ʰ37ᵐ28ˢ85	−24ᵈ30ᵐ01ˢ1	17.22	2.58	NAM[3,4]	44	181	5.9	SB(s)dm pec
NGC 1433	03ʰ42ᵐ01ˢ55	−47ᵈ13ᵐ19ˢ5	18.63[d]	1.86	PNLF[5]	29	200	1.5	(R_1_')SB(r,p,nrl,nb)a
NGC 1512	04ʰ03ᵐ54ˢ28	−43ᵈ20ᵐ55ˢ9	18.83[d]	1.88	PNLF[5]	43	262	1.2	(RL̲)SB(r,bl,nr)a
NGC 1566	04ʰ20ᵐ00ˢ42	−54ᵈ56ᵐ16ˢ1	17.69	2.00	Group[2]	30	215	4	(R_1_')SAB(rs,rs̲)b
NGC 1672	04ʰ45ᵐ42ˢ50	−59ᵈ14ᵐ49ˢ9	19.40	2.91	NAM[3,4]	43	134	3.3	(R')SAB̲(rs,nr)b
NGC 2835	09ʰ17ᵐ52ˢ91	−22ᵈ21ᵐ16ˢ8	12.22	0.94	TRGB[1]	41	1	5	SB(rs)c
NGC 3351	10ʰ43ᵐ57ˢ70	+11ᵈ42ᵐ13ˢ7	9.96	0.33	TRGB[1]	45	193	3.1	(R')SB(r,bl,nr)a
NGC 3627	11ʰ20ᵐ14ˢ96	+12ᵈ59ᵐ29ˢ5	11.32	0.48	TRGB[1]	57	173	3.1	SB_x_(s)b pec
NGC 4254	12ʰ18ᵐ49ˢ60	+14ᵈ24ᵐ59ˢ4	13.1	2.8	SCM[6]	34	68	5.2	SA(s)c pec
NGC 4303	12ʰ21ᵐ54ˢ90	+04ᵈ28ᵐ25ˢ1	16.99	3.04	Group[2]	24	312	4	SAB(rs,nl)bc
NGC 4321	12ʰ22ᵐ54ˢ83	+15ᵈ49ᵐ18ˢ5	15.21	0.49	Cepheid[7]	39	156	4	SAB(rs,nr,nb)bc
NGC 4535	12ʰ34ᵐ20ˢ31	+08ᵈ11ᵐ51ˢ9	15.77	0.37	Cepheid[7]	45	180	5	SAB(s)c
NGC 5068	13ʰ18ᵐ54ˢ81	−21ᵈ02ᵐ20ˢ8	5.20	0.21	TRGB[1]	36	342	6	SB(s)d
NGC 7496[e]	23ʰ09ᵐ47ˢ29	−43ᵈ25ᵐ40ˢ6	18.72	2.81	NAM[3,4]	36	194	3.2	(R')SB_x_(rs)b
IC 5332[e]	23ʰ34ᵐ27ˢ49	−36ᵈ06ᵐ03ˢ9	9.01	0.41	TRGB[1]	27	74	6.8	SA̲B(s)cd

Notes.

[a] Compilation of galaxy distances (D) and uncertainties (σ_D). Distance methods include TRGB (tip of the red giant branch), Group, NAM (numerical action model), PNLF (planetary nebula luminosity function), SCM (standardizable candle method), and Cepheid (Cepheid period–luminosity relation). Superscripts indicate the primary reference given in the compilation by Anand et al. (2021a) and are as follows: (1) Anand et al. (2021b), (2) Kourkchi & Tully (2017), (3) Shaya et al. (2017), (4) Kourkchi et al. (2020), (5) Scheuermann et al. (2022), (6) Nugent et al. (2006), and (7) Freedman et al. (2001).

[b] Galaxy inclination and position angle adopted from Lang et al. (2020) where available and Leroy et al. (2021) otherwise.

[c] Morphological T-type from HyperLEDA (Makarov et al. 2014). Morphological classification from Buta et al. (2015) except for NGC 2835, which comes from de Vaucouleurs et al. (1991).

[d] The PNLF distances to NGC 1433 and 1512 varied from Anand et al. (2021a), which was used in Emsellem et al. (2022) and Leroy et al. (2021), and Scheuermann et al. (2022).

[e] One of the first four galaxies observed that form the basis of the PHANGS–JWST first results presented in this volume.

can identify and characterize individual H II regions, and ALMA resolves the molecular ISM into individual massive molecular clouds and complexes. Meanwhile, the mass and specific SFR criteria select galaxies on the "main sequence" of star-forming galaxies, ensuring that the surveys capture environments that reflect where most stars form at $z = 0$ (e.g., Brinchmann et al. 2004; Salim et al. 2007; Saintonge et al. 2017).

As is typical for surveys of nearby galaxies, our best estimates of the properties of galaxies in the sample have evolved since they were first selected, in particular due to the continuing improvement in distance estimates (Anand et al. 2021a; Lee et al. 2022). As a result, the properties of the parent sample have broadened slightly beyond the original selection criteria, with the result that the PHANGS–JWST sample includes galaxies with distances out to ~20 Mpc and stellar masses as low as ~$2.5 \times 10^9 \, M_\odot$.

In practice, the requirement that PHANGS–JWST galaxies have the full complement of PHANGS–ALMA, MUSE, and HST data means that the PHANGS–JWST selection will be identical to that of the precursor survey with the smallest sample, which is PHANGS–MUSE (Emsellem et al. 2022). PHANGS–MUSE targeted the first 19 galaxies from the PHANGS parent sample for which ALMA CO(2–1) mapping was obtained. The resulting sample satisfies the general goal to provide a reasonably representative selection of massive star-forming galaxies spanning a factor of ~50 in stellar mass and SFR (Figure 3 in Emsellem et al. 2022), morphological types from Sa to Sd with a diversity of bar and ring structures, and a factor of ~100 in CO surface densities (Figure 1 in Lee et al. 2022).

3. JWST Observations

PHANGS–JWST observations for our sample of 19 galaxies are obtained under JWST program 2107 (PI: J. Lee) with a total allocation of 112.6 hr.[69] As mentioned in the Introduction, data for four galaxies (NGC 7496, IC 5332, NGC 628, and NGC 1365) were obtained within the first 2 months of science operations (Table 3) and provide the basis for the first PHANGS–JWST results presented in this Issue.[70] Six more targets are currently scheduled for observations during 2022, and program completion is anticipated in mid-2023.

Imaging is conducted with NIRCam and MIRI in eight filters from 2 to 21 μm (Figure 2). This set of filters is chosen to support our broad science goals (see Section 6), as well as to optimize observing efficiency (more below).

PHANGS–JWST coverage is designed to maximize overlap with PHANGS data already obtained by HST, VLT-MUSE, and ALMA, all of which targeted the main star-forming area of the galaxy disk. This requires one to two pointings with NIRCam (Module B only) and two to four pointings with MIRI for each galaxy. For both NIRCam and MIRI, we use 10% overlap

[69] Accounting for changes in overhead calculations as of 2022 November 19. Approximately 70% of this allocation is spent on observational overheads (e.g., slew times).

[70] Due to a guide star acquisition failure, the NIRCam observations of IC 5332 were not completed and have been rescheduled for later in JWST Cycle 1. Since our observation strategy uses the time when the NIRCam observations are targeting the galaxy to observe the MIRI off-source position "in parallel," our IC 5332 data set also currently lacks an off-source observation for MIRI.

Table 2
PHANGS–JWST Target Galaxy Physical Properties

Galaxy	$\log M_\star$ [a] ($M_\odot$)	SFR_{tot} [b] ($M_\odot\ yr^{-1}$)	R_e [c] (kpc)	$\log_{10} L_{CO}$ [d] (K km s^{-1} pc^2)	$M_{H\,I}$ [e] ($M_\odot$)	$12 + \log_{10} O/H$ [f]	f_{JWST} [g]
NGC 0628 [h]	10.3	1.7	3.9	8.4	9.7	8.53	0.53
NGC 1087	9.9	1.3	3.2	8.3	9.1	8.48	0.88
NGC 1300	10.6	1.2	6.5	8.5	9.4	8.62	0.87
NGC 1365 [h]	11.0	17	2.8	9.5	9.9	8.67	0.76
NGC 1385	10.0	2.1	3.4	8.4	9.2	8.46	0.94
NGC 1433	10.9	1.1	4.3	8.5	9.4	8.57	0.50
NGC 1512	10.7	1.3	4.8	8.3	9.9	8.58	0.46
NGC 1566	10.8	4.6	3.2	8.9	9.8	8.61	0.70
NGC 1672	10.7	7.6	3.4	9.1	10.2	8.57	0.87
NGC 2835	10.0	1.3	3.3	7.7	9.5	8.56	0.46
NGC 3351	10.4	1.3	3.0	8.1	8.9	8.58	0.66
NGC 3627	10.8	3.9	3.6	9.0	9.8	8.54	0.86
NGC 4254	10.4	3.1	2.4	8.9	9.5	8.59	0.90
NGC 4303	10.5	5.4	3.4	9.0	9.7	8.58	0.80
NGC 4321	10.8	3.5	5.5	9.0	9.4	8.56	0.68
NGC 4535	10.5	2.2	6.3	8.6	9.6	8.54	0.57
NGC 5068	9.4	0.3	2.0	7.3	8.8	8.32	0.71
NGC 7496 [h]	10.0	2.2	3.8	8.3	9.1	8.51	0.88
IC 5332 [h]	9.7	0.4	3.6	7.1	9.3	8.30	0.27

Notes.
[a] Galaxy stellar mass. Following Leroy et al. (2021), based on Spitzer IRAC 3.6 μm when available, or WISE 3.4 μm, and the mass-to-light ratio prescription of Leroy et al. (2019) calculated as a function of radius in the galaxy.
[b] Here SFR_{tot} is the total galaxy SFR. Based on GALEX far-UV and WISE W4 imaging with the SFR prescription calibrated to match results from population synthesis modeling of Salim et al. (2016, 2018) as in Leroy et al. (2021).
[c] Stellar mass effective radius from Leroy et al. (2021) and closely resembling the near-IR effective radius (Munoz-Mateos et al. 2015).
[d] Integrated CO (2–1) luminosity. Scale by $\alpha_{CO} \approx 6.7\ M_\odot\ pc^{-2}$ (K km s^{-1})$^{-1}$ to estimate M_{mol} including helium and metals using a fixed CO-to-H$_2$ conversion factor.
[e] Atomic gas mass, not including helium, from HyperLEDA (Makarov et al. 2014).
[f] Gas phase metallicity on the S-cal system (Pilyugin & Grebel 2016) estimated at R_e by Groves et al. (2023).
[g] Fraction of the SFR estimated from the UV+IR that lies within the PHANGS–HST field of view from Lee et al. (2022). This can be applied with reasonable precision to aperture correct the SFR, L_{CO}, or $M_\star$ to estimate the quantity inside the JWST field of view.
[h] One of the first four galaxies observed that form the basis of the PHANGS–JWST first results presented in this volume.

between rows and columns of mosaic tiles. With this setup, 13 galaxies required two pointings with NIRCam (Module B only), while nine were observed with a single pointing. With MIRI, up to four pointings were required, with one, six, three, and nine galaxies requiring one, two, three, and four pointings, respectively. The resultant PHANGS–JWST NIRCam and MIRI footprints are shown in Figure 1.

Total exposure times per pointing in each filter are listed in Table 4 and range from 6.4 to 20 minutes with NIRCam and 1.5 to 5.4 minutes with MIRI. Tables 5 and 6 summarize the observing parameters and exposure sequences adopted for each filter in each visit.

3.1. NIRCam Primary Observations

Our NIRCam primary observations are divided into four separate sequences to maximize observing efficiency (Table 5). This allows for MIRI sky background observations to be taken in parallel with each NIRCam sequence, with one sequence for each of the four MIRI filters in our program. With NIRCam, we use Module B (FULL subarray) and an INTRAMODULE-BOX-4 primary dither pattern with no additional subpixel dither.[71] We obtain four F200W exposures, one at each INTRAMODULEBOX-4 dither position (for a total of 16 exposures), using the BRIGHT1 readout pattern with one

integration per exposure. Of these independent sequences, two have five groups/integration, contributing 386.5 s each to the total F200W exposure time, and the other two have three groups/integration, yielding 214.7 s each. The total F200W exposure time is thus 1202.5 s pointing^{-1}.

Simultaneously with F200W primary imaging in the short-wavelength channel (and coordinated parallel MIRI imaging of sky background), we observe the target with F300M, F335M, and F360M in the long-wavelength channel. The F300M and F335M observations are paired with the two longer F200W exposure sequences. The exposure time for F300M and F335M is consequently 386.5 s (each). During both of the two shorter F200W exposure sequences, F360M imaging is obtained, for a total exposure time of 429.5 s.

3.2. MIRI Primary Observations

For our MIRI primary observations, we use a four-point dither pattern optimized for extended sources. We observe with the F770W, F1000W, F1130W, and F2100W filters and the FASTR1 readout pattern, yielding total exposure times per pointing of 88.8, 122.1, 310.8, and 321.9 s, respectively (Table 6). All of the galaxies are larger than the MIRI field of view, so we obtain a background measurement using this same MIRI imaging sequence for a blank region of sky near the galaxy in parallel with NIRCam, as just discussed.

[71] The primary dither pattern itself has very minimally sampled subpixel dithering.
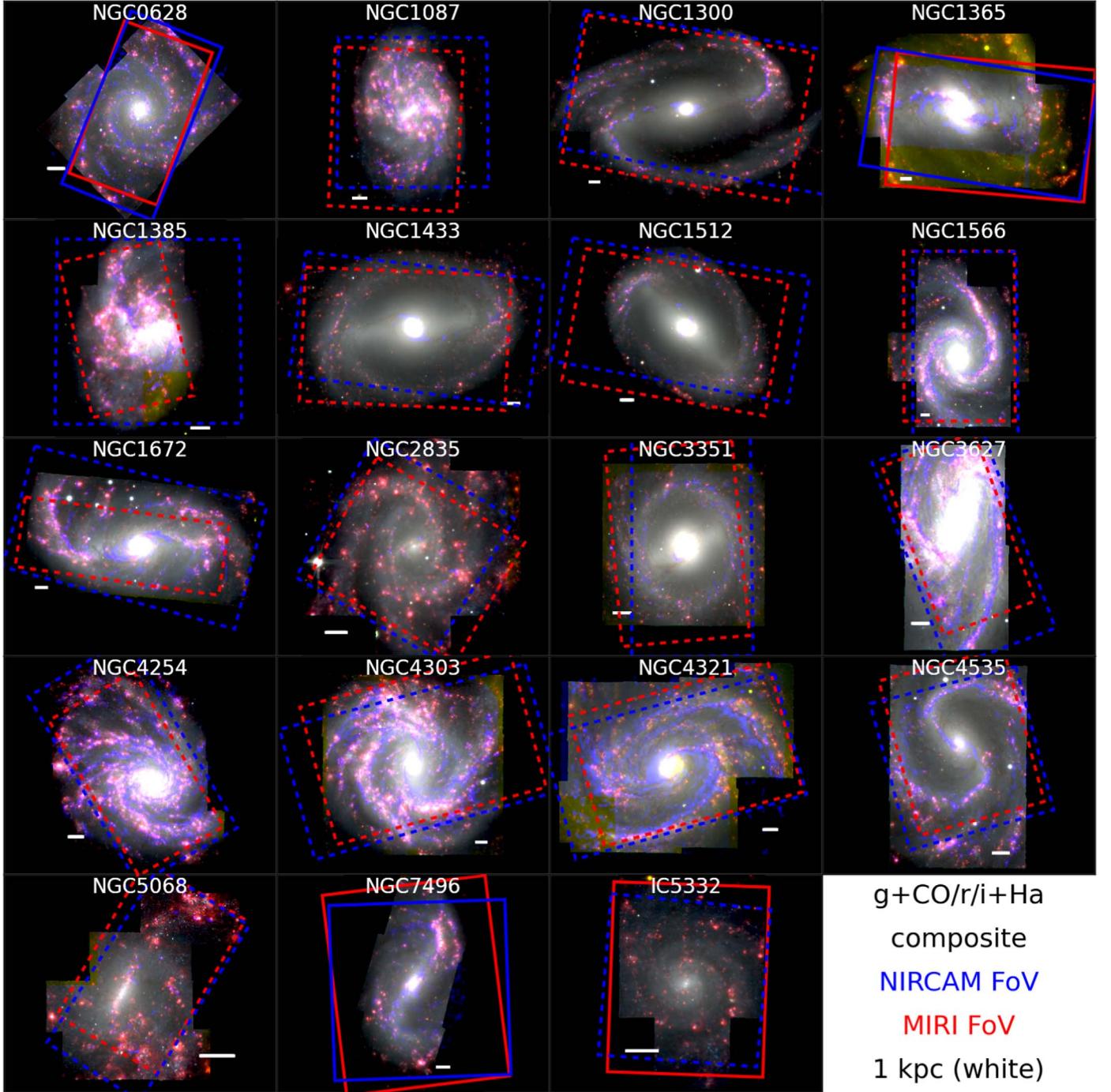
Figure 1. Composite *gri*+Hα+CO images for the 19 galaxies in the PHANGS–JWST Treasury program. The *gri*+Hα images are constructed from VLT-MUSE full-field spectral mapping (Emsellem et al. 2022), with Hα line emission in red, and combined with ALMA CO(2–1) (Leroy et al. 2021) maps, with CO(2–1) flux in blue. The JWST NIRCam and MIRI footprints have been defined to overlap existing MUSE, ALMA, and HST data. Footprints shown with dashed lines represent observations that had not been executed at time of writing (2022 October) and may rotate slightly due to the range of allowed orient angles specified for the target. The JWST sample spans a factor of ∼50 in stellar mass and SFR and a factor of ∼100 in CO surface density (Table 2). It includes galaxies with prominent dust lanes; a full range of stellar bar, bulge, spiral arm morphologies; and nuclear starburst and AGN activity.

3.3. Special Requirements

We include the following special requirements in our observation plan: (1) a timing requirement (sequence observations, noninterruptible) that ensures the MIRI background imaging is obtained directly following the MIRI observation of the target and (2) position angle requirements to maximize the overlap of the primary MIRI observations with existing HST, MUSE, and ALMA coverage, while placing the parallel MIRI

background observation on blank sky. In some of the galaxies with the largest angular extents in our sample, the parallel sky background measurement may not be completely beyond the outskirts of the galaxy disk. Finally, whenever possible, we attempted to widen the orient constraints to provide a minimum observation window of 2 weeks to provide greater opportunities for scheduling. It should be noted that the range in allowable orient angles can result in imaging that is not
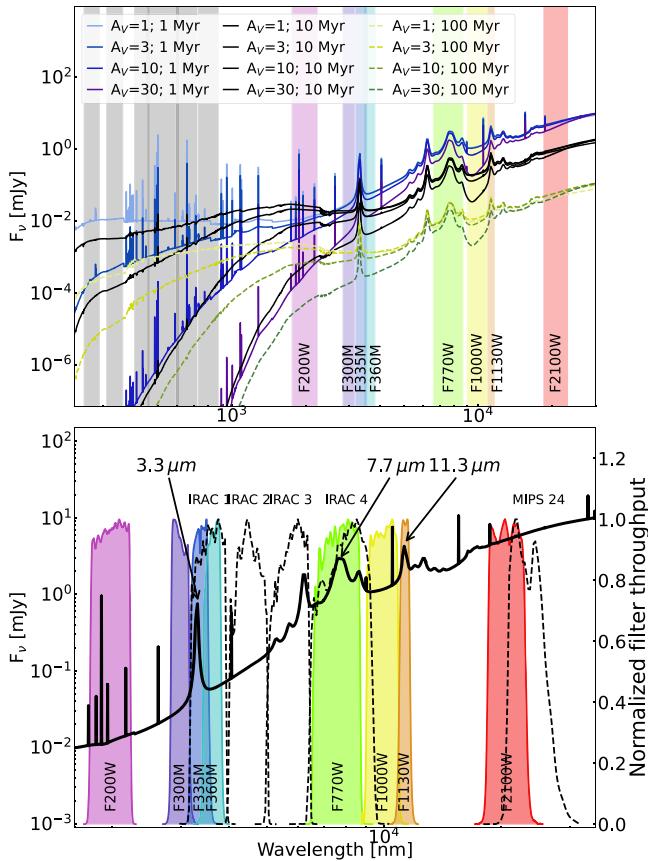
Figure 2. Top: model SEDs of dust-enshrouded young star clusters with filter coverage of the PHANGS–HST and JWST Treasury programs. Models are of a solar metallicity $10^4 \, M_\odot$ young star cluster at $d = 10$ Mpc with varying ages and levels of extinction generated with CIGALE (Boquien et al. 2019; Turner et al. 2021). Colored bands show the eight JWST NIRCAM and MIRI filters, spanning from 2 to 21 μm, selected to probe stellar photospheric emission, PAH features, and the dust continuum. The five UV-visible filters used by PHANGS–HST (Lee et al. 2022) appear in gray. Bottom: normalized throughput for each of the eight filters used in the PHANGS–JWST survey. For comparison, the four Spitzer IRAC filters and MIPS 24 μm filter are also shown. A model dust SED is overplotted to illustrate the features probed by each filter. The three PAH features targeted by our survey are marked.

Table 3
PHANGS–JWST First Results Observations

Galaxy	MIRI Obs. Date (UT: 2022)	NIRCam Obs. Date (UT: 2022)
NGC 7496	7/6 18:02–19:45	07/06 19:50–20:51
IC 5332	7/6 21:05–22:48	…
NGC 0628	7/17 12:14–14:47	07/17 15:01–17:03
NGC 1365	8/13 15:00–16:43	08/13 18:33–20:35

optimally aligned with previous data or astrophysically interesting features in the galaxy. For example, in NGC 1365, the observed orientation led to the omission of portions of the eastern spiral arm.

4. Initial Image Processing

In this section, we describe how the STScI JWST Science Calibration Pipeline[72] is used with additional processing to enable a first set of analyses by the PHANGS team. We completed processing of the images for the papers presented in this Issue by early 2022 September. The latest versions of the pipeline and calibration files available at the time of processing were used: version 1.7.0 (for MIRI) and 1.7.1 (for NIRCam) of the JWST pipeline and Calibration Reference Data System[73] (CRDS context number 0968 for both NIRCam and MIRI, though for MIRI, we used slightly updated flats provided by K. Gordon).

4.1. Level One Processing

We start with the uncalibrated raw ("uncal") files obtained from the Mikulski Archive for Space Telescopes (MAST) and use Detector1Pipeline, which converts from "ramps" to "slopes" and applies basic detector-level corrections to the data, including the flagging of saturated pixels and corrections for chip persistence.[74] We ran the Detector1Pipeline with the default parameters, with one exception. To attempt to recover some of the saturated pixels, we removed the restriction that during ramp fitting, at least two groups must not reach saturation. These saturated pixels are primarily an issue in the centers of NGC 1365 and NGC 7496, which both host bright active galactic nuclei (AGN). Removing the restriction did not recover the very central pixels coincident with the AGN themselves, but it did allow us to recover a number of the brighter pixels surrounding the central point source. However, some of these sources, especially the brightest compact, massive star-forming regions in the starburst ring of NGC 1365, still show artifacts that have structure suggesting that the source brightness remains underestimated by the imaging.

4.2. Level Two Processing

Stage two of the pipeline produces calibrated individual exposures.[75] During this stage, the pixel coordinates are translated into WCS coordinates, which includes application of distortion corrections. This stage also involves flat-fielding and background subtraction (the background subtraction is used only for the MIRI data). Because of our parallel observing visit sequence (Section 3), the pipeline does not automatically associate the appropriate MIRI off (sky background) observations with the on-galaxy images. Instead, we manually implement this association during this processing step. For IC 5332, only the on-galaxy MIRI observations were obtained during our initial visit. Therefore, we used the off-galaxy observation from NGC 7496 for this purpose in IC 5332. This appears to work reasonably well but does result in a few visible imperfections in the background subtraction for IC 5332. Also for MIRI, we masked the part of the image associated with the Lyot coronagraph. In this early reduction, the coronagraph portions of the image consistently showed imperfect background subtraction that caused issues with our mosaicking.

4.3. Principal Component Analysis Destriping

After stage two, we applied additional processing to suppress $1/f$ noise in the NIRCam data. This correlated read noise primarily manifests as striping across the NIRCam images

---

[72] https://github.com/spacetelescope/jwst

[73] https://jwst-crds.stsci.edu/
[74] https://jwst-pipeline.readthedocs.io/en/latest/jwst/pipeline/calwebb_detector1.html
[75] https://jwst-pipeline.readthedocs.io/en/latest/jwst/pipeline/calwebb_image2.html

Table 4
Total Exposure Times, Resolution, and Sensitivities for PHANGS–JWST NIRCAM and MIRI Imaging

Filter	FWHM (arcsec)	FWHM (pixels)	N_{exp}	Exp. Time (s)	Ω_{PSF}[a] $(10^{-12}$ sr)	σ_I[b] (MJy sr^{-1})	$5\sigma_f$[c] (μJy)
NIRCam							
F200W	0.066	2.141	16	1202.5	0.167	0.068	0.079
F300M	0.100	1.585	4	386.5	0.365	0.045	0.077
F335M	0.111	1.760	4	386.5	0.458	0.042	0.10
F360M	0.120	1.901	8	429.5	0.530	0.058	0.17
MIRI							
F770W	0.25	2.27	4	88.8	2.18	0.11	0.87
F1000W	0.32	2.91	4	122.1	3.77	0.12	1.9
F1130W	0.36	3.27	4	310.8	4.95	0.15	2.4
F2100W	0.67	6.09	8	321.9	16.1	0.25	8.0

Notes.
[a] The solid angle subtended by the PSF, calculated using the WEBBPSF package (Perrin et al. 2014).
[b] The empirical 1σ surface brightness sensitivity σ_I estimated directly from the image data (Section 5.2). This estimate agrees well with the pipeline-provided noise products.
[c] The 5σ point-source sensitivity ($5\sigma_f$) based on empty apertures in low-brightness regions of the image. See Section 5.2.

along detector rows (in the fast-read direction). This can severely degrade the quality of the images, particularly at shorter wavelengths. Schlawin et al. (2020) studied this effect using simulated data and provided a number of suggestions for how to deal with this $1/f$ noise. We experimented with simple row-by-row median subtraction but found that it was often unfeasible to calculate a robust background median in the small range covered by each amplifier due to the presence of widespread diffuse emission in most of our images. Moreover, we found that though this median subtraction produced visually better individual images, it yielded poor results when multiple images were combined to estimate $3.3\,\mu m$ PAH maps (Sandstrom et al. 2023a). In those cases, the $1/f$ noise-driven stripes reappeared and were severe in the star-subtracted PAH images.

Instead, as shown in Figure 3, we had success modeling the $1/f$ noise using robust principal component analysis (PCA) based on the technique developed in Wild & Hewett (2005) and Budavári et al. (2009) for SDSS spectra. We treat each column of the data as an individual noise spectrum and fit the results for each amplifier separately because the noise properties differ between amplifiers. We mask out bright sources and then apply a Butterworth (1930) filter to remove large-scale structure but retain the small-scale noise properties. We also shuffle in the x-direction and apply a different offset to each column, effectively rolling the column along the y-axis by a random amount. These shifts prevent the PCA from simply learning where the mask is and responding to the location of bright emission. After this processing, we use PCA to fit 50 components. Then we reconstruct a model describing the $1/f$ noise-induced stripes for that column using the five components with the largest eigenvalues. Using only five components limits the processing time, and we found that increasing the number of components beyond five did not significantly improve the noise model. Finally, we subtract the model of the $1/f$ noise-induced stripes from the data.

Figure 3 illustrates this process. The left image shows visible artifacts, mostly horizontal striping. The PCA model successfully captures these features without including the extended bright emission from the source. Occasionally, corrupted columns and other features arise, which the PCA also robustly handles. The right image shows visibly less striping and fewer

artifacts than the original image. We find that the PCA reduces the rms noise in the images between around 10% and 30%, with the amount of reduction depending mainly on the amount of area filled by emission in the image. For images with more source-free sky background, the PCA produces a more significant decrease in the noise level.

4.4. Level Three Processing

The level three stage of the pipeline[76] is intended to combine individual tiles to produce a final rectified mosaic. This is achieved through relative alignment between tiles, background matching, and the final drizzling to the output pixel grid.

In our early science reduction, this step involved the most changes from the default pipeline parameters. For MIRI, we ran the level three pipeline on individual tiles, i.e., the individual pointings, which we later mosaicked together by hand. For NIRCam, we used the JWST pipeline to stitch the tiles.

We adjusted the stage three pipeline as follows. First, in the `tweakreg` step, which provides relative alignment between tiles, we found it necessary to limit the "roundness" of sources used for alignment to $-0.5 <$ roundness < 0.5 to reject diffraction spikes from stars and the numerous extended sources in our field. We also turned off the `2dhist` option, as our relative corrections were generally $\lesssim 1''$, and leaving this on degraded the quality of the alignment. We fit the per-tile offsets using only (x, y) shifts, as we found that allowing for rotation produced negligible rotation angles and degraded the quality of the fits. For data acquired in 2022 July and August, we found relative corrections as large as $\sim 1''$. This primarily reflects the quality of the guide star catalog during that period. The size of the correction will likely decrease as JWST observations continue and the guide star catalog is updated and improved.

For the NIRCam data, we calculate and subtract the background level for each detector individually. By default, the pipeline will subtract a single background for the four short-wavelength NIRCam detectors; however, we found that this produced clear "steps" in our mosaics.

---

[76] https://jwst-pipeline.readthedocs.io/en/latest/jwst/pipeline/calwebb_image3.html

Table 5
NIRCam Primary Observation and MIRI Background Parallel Visit Plan

			INTRAMODULEBOX Pattern with Four Primary Dithers, BRIGHT1 Readout Pattern				
NIRCam Short Filter	NIRCam Long Filter	Grp./Int.	Int./Exp.	Exp. Time (s)	MIRI Bkgd. Filter (in parallel)	Grp./Int.	Int./Exp.	Exp. Time (s)
F200W	F360M	3	1	214.7	F770W	8	1	88.8
F200W	F360M	3	1	214.7	F1000W	11	1	122.1
F200W	F300M	5	1	386.5	F1130W	28	1	310.8
F200W	F335M	5	1	386.5	F2100W	14	1	321.9

Table 6
MIRI Primary Observation Visit Plan

	Four-point Extended Source Dither Pattern FASTR1 Readout Pattern		
MIRI Filter	Groups per Integration	Integs. per Exposure	Exp. Time (s)
F770W	8	1	88.8
F1000W	11	1	122.1
F1130W	28	1	310.8
F2100W	14	2	321.9

In the final redrizzling step during stage three, we produced mosaics with the conventional north-up orientation to allow for more straightforward comparison with data at other wavelengths.

4.5. Absolute Astrometric Alignment

The level three pipeline produced mosaics that have good relative alignment between NIRCam tiles, but the alignment of the JWST images relative to other data with well-established absolute astrometry tended to be poorer, as high as ∼1″ in some cases. After stage three processing, we therefore performed an additional correction to improve the absolute astrometry of the NIRCam and MIRI images. We adopt the general strategy of bootstrapping the astrometric solution from images that are close in wavelength instead of directly using astrometric catalogs, as was followed for PHANGS–HST (Lee et al. 2022).

Our JWST images lack enough Gaia (Gaia Collaboration et al. 2016) sources to anchor our astrometry directly to Gaia (Lindegren et al. 2018, 2018). However, our NIRCam images detect many asymptotic giant branch (AGB) stars that are also visible in the PHANGS–HST images, which have astrometric solutions accurate to better than 10 mas. Thus, we extracted a set of AGB stars from the PHANGS–HST DOLPHOT catalog (Lee et al. 2022; Thilker et al. 2022) and cross-matched them to sources detected in the NIRCam bands in the level three source_catalog step (the final level three step) using the XYXYMatch function in tweakwcs. Typically, we identified a few hundred AGB stars per target from the PHANGS–HST catalogs, and the pipeline found 50–100 good matches in the NIRCam imaging. We then solve for a linear offset and rotation to match the images (though the rotation was typically very small). After applying these solutions, comparisons between the NIRCam and HST data show that the rms scatter in the astrometric accuracy across the NIRCam images is about ±0.1 NIRCam pixel.

The MIRI images have fewer point sources than those from NIRCam and HST, so we derive the astrometric solution for MIRI using a cross-correlation approach. To do this, we take advantage of the fact that the F335M NIRCam band, which has been anchored using AGB stars to the PHANGS–HST and Gaia frame, contains both stellar and ISM-like emission because of the strong PAH band at 3.3 μm (see Figure 2). The stellar emission allows us to pin the astrometry to the AGB stars and the PHANGS–HST frame, while the morphology of the ISM at 3.3 μm resembles the ISM emission in the longer-wavelength MIRI bands. This allows us to use a cross-correlation analysis to solve for the relative astrometry of the NIRCam and MIRI bands. Specifically, we used the image-registration package to run a cross-correlation and solve for the linear shift (by identifying the maximum of the cross-correlation) needed to match the shortest MIRI band, F770W, to the F335M astrometry. Then, with the F770W astrometry established, we solved for the shift needed to align F1000W to F770W, F1130W to F1000W, and F2100W to F1130W. We adopted this stepwise approach to reflect the increasing dominance of the ISM emission over stellar emission as the wavelength increases. The cross-correlation technique generally produces "good" results but can be sensitive to artifacts, e.g., diffraction spikes around the AGN. By eye, this seems to yield images that are aligned at the level of ±1 MIRI pixel, i.e., about 0″.1. While this is sufficient for the first results presented in this Issue (except where noted in specific papers), the alignment is not as good as would be expected based on alignment based on a more limited set of carefully selected, bright, isolated point sources (e.g., Lee et al. 2022). We expect to significantly improve this in future work.

4.6. By-hand MIRI Mosaicking for Early Science

After level three processing and alignment, we combined the individual MIRI tiles into a single image for each galaxy at each band. To do this, we defined one of the tiles for each galaxy as the reference tile. Then, we reprojected the other tiles onto the astrometric grid for the reference tile and compared the intensity of the two tiles in the region where they overlap. We solved for and applied the additive offset needed to yield a one-to-one match in intensities between the other tile and the reference file. These offsets were typically ≲0.05 MJy sr^{-1} for F770W and F1000W, ≲0.15 MJy sr^{-1} for F1130W, and as high as ∼0.3–0.8 MJy sr^{-1} for F2100W. This yielded a set of individual tiles with the same background level but did not anchor that background level to the correct absolute value.

Next, we defined a new astrometric grid with a larger size but the same pixel scale and orientation as that of the reference field. We then reprojected all tiles onto this new grid, averaging intensities from different tiles with equal weighting where tiles overlapped. The result at this stage was a single combined MIRI image registered via cross-correlation to the NIRCam and

Original Data   Noise Model   Destriped Data
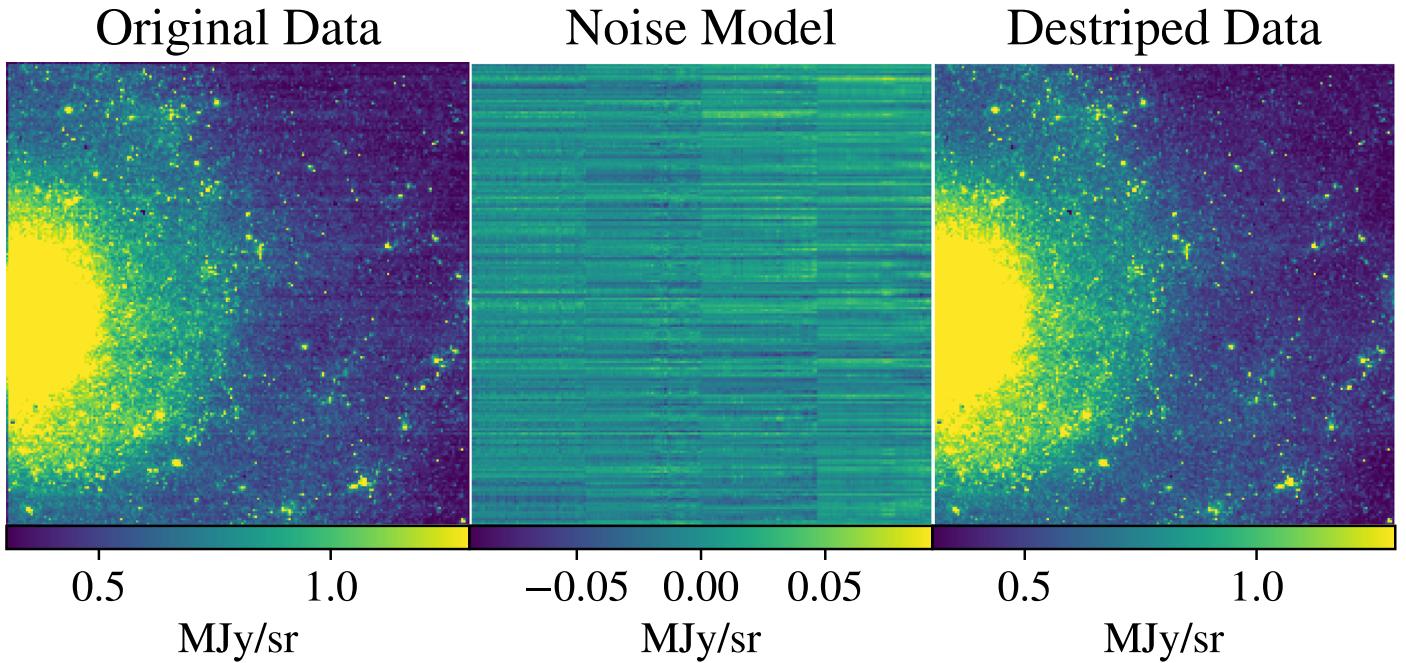
Figure 3. Left: original calibrated image, presented with a strong intensity transfer function to highlight stripes due to $1/f$ noise. Middle: PCA noise model, with the displayed intensity range now centered on zero and the intensity scale boosted by a factor of 5 compared to the original image. Right: final destriped data.

other MIRI images but with an absolute background level that was still uncertain.

Note that we expect to deprecate most of these manual steps as the pipeline processing improves in the future. However, for this first processing during these early months, we found that this simple, by-hand approach yielded smoother backgrounds and a better match to previous infrared imaging of our targets than the pipeline.

4.7. Refinements to the Pipeline Background Subtraction

As a final step, we adjust the overall background level of the MIRI images to match previous wide-field mid-infrared imaging of our targets. The JWST field of view for most of our targets contains relatively little empty sky, and the match between the off-source and on-source image was not sufficient to yield a precise background level. Fortunately, all of our sources have previous observations at least by the Wide-field Infrared Survey Explorer (WISE) at 12 and 22 μm (Wright et al. 2010) and for NGC 628, NGC 1365, and IC 5332 by Spitzer at 8 and 24 μm (Kennicutt et al. 2003; Armus et al. 2009; Dale et al. 2009). Though these data have much worse resolution than the JWST images, they cover a much larger area and extend to empty sky and so have well-established background levels.

We perform this background homogenization in two stages following a procedure detailed in the Appendices of Leroy et al. (2023). First, we establish a common background system across all JWST bands. Then, we anchor the overall system to an external band with a well-established background. To do this, we make a version of the MIRI images that all share the PSF of the F2100W image and a version of all JWST, Spitzer, and WISE data that share a common 15″ FWHM Gaussian PSF. That is, we match the backgrounds among the JWST bands at common resolution. These procedures leverage the fact that mid-infrared emission at different wavelengths shows strong, often nearly linear correlations even though the exact

band ratios vary with filter combination (see the Appendix in Leroy et al. 2023). This procedure appears to yield good results with an uncertainty in the overall background level of better than ± 0.1 MJy sr^{-1} across all MIRI bands.

4.8. Limitations, Caveats, and Expected Improvements

The reduction procedures described above yield data that are useful for the initial work presented in this Issue. Over the longer term, improvements will be made to address known limitations that we summarize here (as well as possible additional issues found during future analysis). In addition to refining our own procedures, we expect to take full advantage of the monthly refinements to the pipeline being released by STScI.[77] The pipeline documentation already identifies some of these issues as areas of future development.

Where these limitations affect our first results scientific papers, they are noted, but most of our analyses are conducted to mitigate their impact. For example, aperture photometry with local background subtraction avoids uncertainties in measurement of the background (e.g., Rodriguez et al. 2023; Whitmore et al. 2023b).

4.8.1. Astrometric Uncertainties

The relative alignment of the NIRCam images is excellent, with sufficient numbers of common sources available in adjacent bands to align frames and tie to the astrometry established in the PHANGS–HST imaging[78]; doi:t9-r08f-dq31. Using AGB stars, we can achieve <10 mas astrometric accuracy for the NIRCam data (Section 4.5). The MIRI images are currently aligned by cross-correlation and have a larger uncertainty in their astrometric solutions ($\pm 0\rlap{.}''1$).

---

[77] https://jwst-docs.stsci.edu/jwst-science-calibration-pipeline-overview/jwst-operational-pipeline-build-information
[78] https://archive.stsci.edu/hlsp/phangs-hst

We expect that a combination of better constraints from cross-correlation and the use of AGB stars will increase the astrometric accuracy of the MIRI images. Astrometric solutions are also expected to continue to improve as distortion models are updated by STScI.

Our science images are not currently drizzled onto a matched pixel grid, but adopting and drizzling to the grid adopted for the PHANGS–HST images would significantly facilitate joint HST–JWST analysis. However, the different pixel scales spanned from 2 to 21 μm make this exercise a trade-off between retaining information and limiting data volume.

4.8.2. Flux Calibration and Backgrounds

The zero-points (i.e., absolute flux calibration) for the JWST instruments are being refined. These changes will primarily affect the NIRCam data (Boyer et al. 2022), and shortly after the completion of the analyses presented in this volume, these zero-points were updated by STScI.

The background levels of the MIRI data have been inferred from band-to-band correlations and comparison with existing lower-resolution infrared imaging from previous missions. These are currently uncertain at the ± 0.1 MJy sr^{-1} level. Comparison of the MIRI data with previous data indicates that, after the subtraction of a background, the intensity measurements agree to better than 10%.

We expect that the mosaicking and tiling in the pipeline will improve and replace our by-hand approach to the MIRI data. In addition to yielding a better astrometric solution, this will allow rigorous testing of the pipeline noise estimates and move us toward an accurate noise model for MIRI. As improved flats and better sky-subtraction techniques become available, they should also improve the local behavior of the MIRI backgrounds.

4.8.3. Saturation and Poor Ramp Fitting

Some of the brightest sources in the MIRI imaging, particularly in NGC 1365, are saturated and show artifacts resulting from poor ramp fitting, and the surrounding areas are affected by diffraction spikes. The photometry of sources with poor ramp fits is likely underestimated (Section 4.1).

Hassani et al. (2023) produced bespoke masks to flag diffraction spikes due to the AGN in NGC 1365 and NGC 7496, but as better PSF estimates become available, subtracting such features from the image should become an option. Liu et al. (2023) presented the first efforts at recovering the fluxes of sources with saturated pixels and poor ramp fits by using PSF matching in the outskirts of the source.

4.8.4. Angular Resolution

Finally, while not strictly an image processing issue, we caution that the large span of wavelengths of our JWST images implies a similar variation in their angular resolution. Analysis that involves comparisons across multiple JWST bands, or between the JWST and other data, requires care to ensure that relative flux measurements are robust. In general, the analyses in this volume rely on flux density measurements from aperture photometry or on surface brightness comparisons, generally at matched resolution. Where appropriate, we have generated convolution kernels following the method of Aniano et al. (2011) to degrade the resolution of short-wavelength images to the long-wavelength bands, achieving a common resolution

match. In the future, PSF-fitting packages like DOLPHOT (Dolphin 2016) will be used, and methods to employ joint spectral energy distribution (SED)/image deconvolution based on priors from the higher-resolution short-wavelength imaging will be implemented. However, the results presented in this volume rely on simpler methods and should be interpreted accordingly.

5. Overview of First PHANGS–JWST Images

5.1. Comparison to Spitzer

While past infrared missions have provided imaging of the nearby galaxies in the PHANGS–JWST sample, JWST's vast improvement in sensitivity and resolution reveals an extraordinary new view of the complex organization of the ISM. In Figures 4 and 5, we present our JWST imaging of NGC 628 and NGC 7496 in selected filters alongside previous Spitzer observations to illustrate data quality and the new science enabled by the observations. The two galaxies are at 9.84 and 18.7 Mpc, respectively, and span most of the distance range (5–20 Mpc) covered by our sample. In Figure 2, we show the filter curves of the Spitzer bands that overlap JWST wavelength coverage together with the eight PHANGS–JWST filters.

Perhaps the most remarkable feature in the PHANGS–JWST imaging is the network of filaments, shells, and bubbles and the star-forming populations nested in these structures, as traced by the dust in emission. While the highest surface brightness features are apparent in the Spitzer imaging, the JWST imaging shows the pervasiveness of the network deep into the interarm regions and morphological details that suggest that the multiscale impact of star formation feedback on the ISM is ubiquitous. With the PHANGS–JWST imaging, we will now be able to develop catalogs of these structures and characterize their ensemble properties (e.g., Hassani et al. 2023; Rodriguez et al. 2023; Thilker et al. 2023; Watkins et al. 2023) even with the lowest-resolution image at 21 μm.

For both NGC 628 and NGC 7496, we show the NIRCam F335M and Spitzer/IRAC 3.6 μm images. The NIRCam F335M filter better isolates the 3.3 μm PAH feature, and observations in the flanking F300M and F360M bands (not shown) enable continuum subtraction. It is clear that the increase in resolution (PSF FWHM 1$\overset{\prime\prime}{.}$6 versus 0$\overset{\prime\prime}{.}$11), which now samples 5 pc at NGC 628 and 10 pc at NGC 7496, enables the study of individual star clusters and associations and allows embedded stellar populations to be identified. A slightly extended point source southeast of the galactic center in NGC 628 is resolved into two background galaxies and illustrates how JWST significantly improves the characterization of extended stellar structures and the identification of background "interlopers."

For NGC 628, the MIRI F770W and Spitzer/IRAC 8 μm images are shown. The bandpasses, which are similar, capture the complex of PAH features in the ~8 μm spectral region (Figure 2). Overall, the same structures are apparent in both images, with the MIRI F770W image being eight times sharper (PSF FWHM 2$\overset{\prime\prime}{.}$0 versus 0$\overset{\prime\prime}{.}$24), sampling 12 pc at NGC 628.

Finally, the MIRI F2100W and Spitzer/MIPS 24 μm images, which capture flux from the warm dust continuum, are shown for both galaxies. Here, although the relative increase in the angular resolution is similar to that for the previous two sets of images, the improvement in the fidelity of the JWST data is the most dramatic, as the MIPS 24 μm PSF
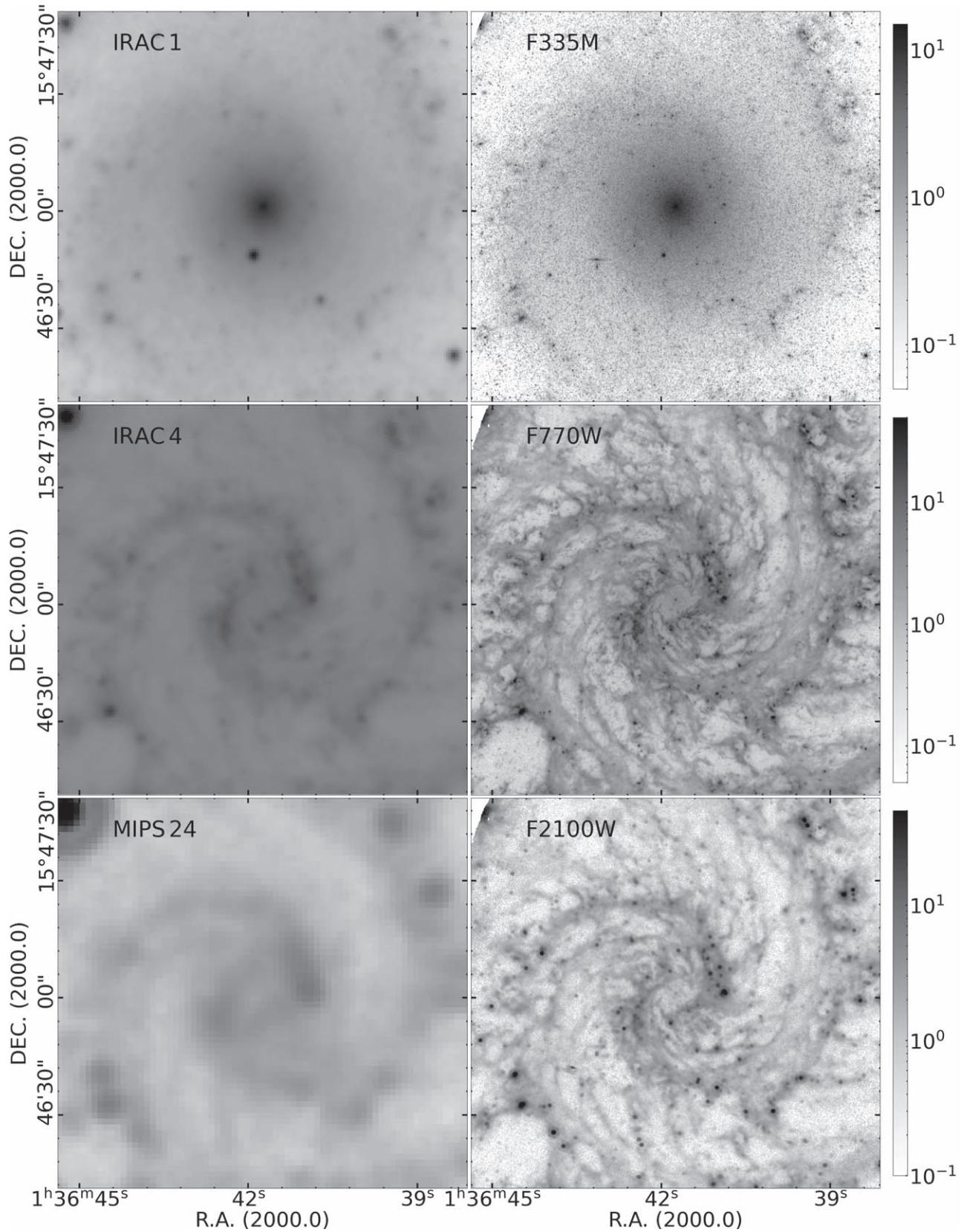
Figure 4. New PHANGS–JWST imaging for NCG 628 (right panels) compared with data previously taken with Spitzer (left panels), illustrating the order-of-magnitude gains in resolution and sensitivity. Comparisons at three different wavelengths are shown. Top panels: Spitzer IRAC 3.6 μm (channel 1) vs. JWST NIRCam F335M. Middle panels: Spitzer IRAC 8 μm (channel 4) vs. JWST MIRI F770W. Bottom panels: Spitzer MIPS 24 μm vs. JWST MIRI F2100W. The Spitzer IRAC and MIPS data are taken from the SINGS program (Kennicutt et al. 2003; Dale et al. 2005). The JWST image is formed from a mosaic of two pointings with NIRCam and three pointings with MIRI.
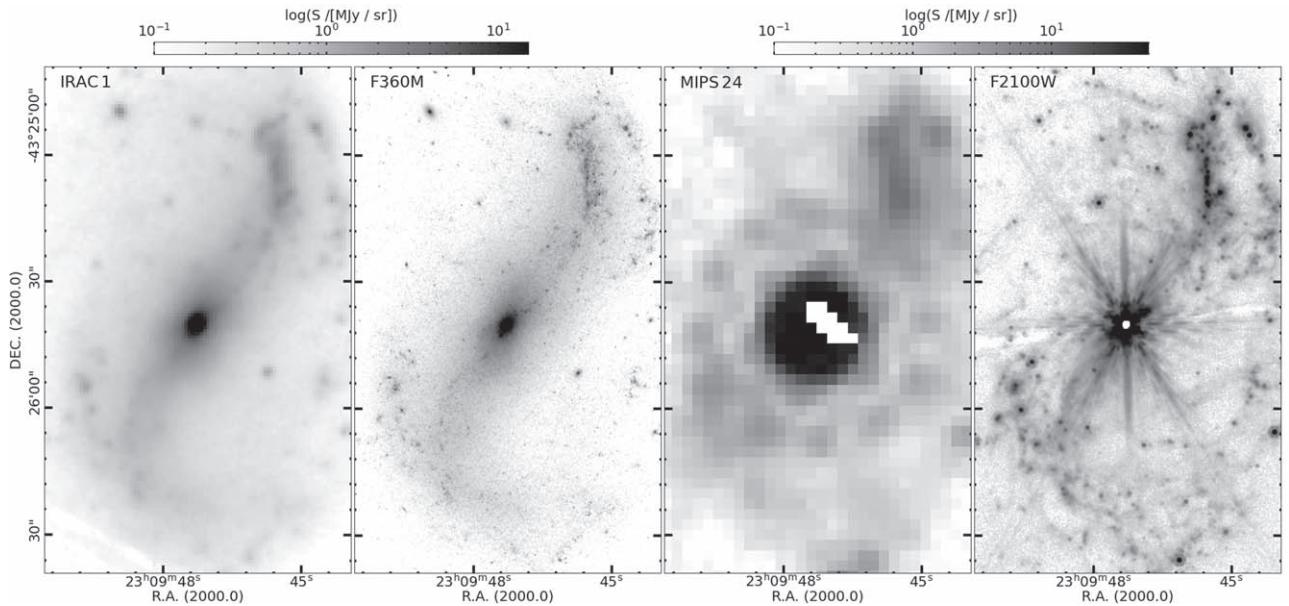
Figure 5. Comparison of new PHANGS–JWST imaging with data previously taken by Spitzer, now for NGC 7496. Here comparisons at two wavelengths are shown. Left two panels: Spitzer IRAC 3.6 μm (channel 1) vs. JWST NIRCam F335M. Right two panels: Spitzer IRAC 8 μm (channel 4) vs. JWST MIRI F770W.

was only 6″, and the majority of emission appeared diffuse. With the MIRI F2100W PSF of 0.″67 (30 pc at NGC 628 and 60 pc at NGC 7496), the dust emission is resolved into compact sources, mostly along the spiral arms, and shows the same intricate ISM structure seen in the MIRI F770W image.

In terms of surface brightness, the Spitzer images achieve slightly better sensitivities than the JWST data, as might be expected. The NGC 628 images from the Spitzer SINGS program (Kennicutt, Jr. et al. 2003) are mosaics with 1σ surface brightness limits of $\sim$0.02 MJy sr^{-1} at 3.6 μm and $\sim$0.2 MJy sr^{-1} at 24 μm. The corresponding sensitivities are 0.04 MJy sr^{-1} for NIRCam F335M and 0.25 MJy sr^{-1} for MIRI F2100W (see Table 4 and discussion in the next section). Of course, the principal gain is in the $\sim$tenfold improvement in resolution and the corresponding decrease in the solid angle subtended by the PSF, so that the JWST point-source sensitivity is $\sim$50 times better than Spitzer.

5.2. Empirical Noise Estimates

Table 4 provides sensitivity limits based on our initial reduction of PHANGS–JWST data. We evaluated the depth of our data with respect to detection of point sources at the resolution achieved in each filter and measurement of diffuse emission on a fixed larger scale.

For the point-source limit, we first identified the faintest area mapped that was also fully contained within the footprint of maximum exposure time. Inside each area, aperture photometry was performed for a set of 50 independent circular apertures sized to match the 50% encircled energy radius of each filter. Background estimation for each aperture was also filter-dependent, using an annulus spanning a radial range from two to three times the aperture radius. The sigma-clipped standard deviation of the background-subtracted flux for these "empty" apertures was then scaled by a factor of 10 to estimate the 5σ point-source detection limit in each filter ($5\sigma_f$), which accounts for a factor of 2 for the choice of 50% enclosed energy radius and a factor of 5 for the choice of significance level. No correction was made for the contribution of the point-

source flux to the background annulus flux, which is expected to be negligible for an unresolved source. Averages of these galaxy-specific limits per filter are tabulated. It is important to note that this method does not include loss of point-source sensitivity due to source crowding in more complex, brighter regions of each JWST target. Such loss of completeness due to crowding and the associated photometric bias will be quantified later when PSF-fitting photometry is undertaken for our entire set of targets.

To estimate the surface brightness sensitivity (σ_I) for the imaging data, we consider the distribution of pixel values in an unsharp masked image. For each image, we compute a median filter with a circular top-hat filter with a diameter six times the PSF FWHM in the band. We subtract off the median smoothed version from the original map to remove large-scale structure and produce an unsharp masked image. We then use a median absolute deviation estimator to measure the local noise in the unsharp masked image. We iteratively reject all values larger than the local 3σ noise measurement in each filter. After the data rejection converges, the local noise estimates are smoothed with a top-hat filter that has a size of $15\times$ the PSF FWHM and interpolating over missing values. We compare this local estimate of the noise to the noise estimates provided by the JWST imaging pipeline. The resulting noise maps are within 10% of the pipeline-generated noise maps. We also estimated the local noise by calculating the median autocorrelation of the data as a function of scale and examining the distributions of the data in signal-free parts of the images (though some bands show emission across the field). All methods arrive at similar noise estimates and reflect the spatial structure in the mosaicked fields.

Note that because of the extended JWST PSFs, there is less encircled light at a PSF FWHM than for a Gaussian source. Thus, the simple scaling of surface brightness noise to obtain a point-source sensitivity leads to an overestimate of the point-source sensitivity: $\sigma_I \Omega_{\text{PSF}} \gtrsim \sigma_f$, where Ω_{PSF} is the solid angle subtended by the PSF.

Figure 6. Animation illustrating dust emission in NGC 7496 (JWST MIRI composite in red hue—red: F2100W; green: F1130W; blue: F1000W) relative to stellar continuum emission and dust absorption in the UV-optical (HST WFC3 composite: red: F814W/F555W/F438W; green: F336W; blue: F275W—data available on MAST, doi:10.17909/t9-r08f-dq31). Both images produced by J. Schmidt.

(An animation of this figure is available.)

5.3. Color Composites and Public Outreach

Since the first observations were taken for the PHANGS–JWST Treasury survey in 2022 July, color composites that combine JWST imaging from multiple filters have been developed and released for all of our targets by astronomers, professional public outreach teams, the press, and the public. The color images have broadly captured the attention of both the science community and general public, not only because the structures portrayed are aesthetically stunning but also because the images vividly illustrate and make qualitatively accessible the physics of star formation, feedback, and the ISM, particularly when the UV-optical imaging from HST is included.

Figure 6 shows the first composite PHANGS–JWST image published for NGC 7496, which was observed shortly after the end of commissioning and among the first science data to be released from the mission. The image is a sum of two composites: one based on the HST UV-optical filters (red: F814W/F555W/F438W; green: F336W; blue: F275W) and a second based on the JWST MIRI F1000W, F1130W, and F2100W filters in red hue. The animation compares the emission from the HST and JWST data. The regions and structures that are dark in the optical due to dust obscuration are illuminated in the mid-infrared by the reradiated emission from small dust grains. The complex network of filaments, bubbles, shells, and compact sources described earlier can now be seen in the context of the visible young stellar populations that line the peripheries of the network and have provided the feedback energy that, together with galactic dynamics, shapes the ISM. Infrared compact sources without optical counterparts can be identified, revealing the sites of the earliest stages of star formation.

Figures 7 and 8 show RGB color composites, now based on only the MIRI imaging, for all four PHANGS–JWST first results galaxies. The diversity of the dust emission structure motivates the study of a representative sample of galaxies and our specific science goals (next section). The four galaxies bracket the full range of star formation properties in the sample (with NGC 1365 having the highest star formation activity and gas surface density and IC 5332 among the lowest) and feature varied dynamical structures (e.g., bars in NGC 1365 and NGC 7496, strong spiral arms in NGC 628, and weak spiral structure in IC 5332). The PHANGS–JWST team is collaborating with image processor Judy Schmidt to produce color composites as new data are received and with the public outreach offices at ESA and STScI to support the communication of new results.

6. PHANGS–JWST Science Goals

In this section, we summarize the science goals that motivate the PHANGS–JWST survey and highlight how the results presented in this Issue begin to make progress toward those goals.

Our studies of star formation and dust emission on the scales of star clusters, H II regions, and giant molecular clouds are enabled by JWST's new high-resolution views of the near- and mid-IR in our selected set of eight filters. As shown in Figures 2 and 9, the F200W, F300M, and F360M filters provide low-obscuration views of stellar photospheric emission, with some contribution from nebular emission and hot dust. The F335M, F770W, and F1130W capture PAH emission, tracing a combination of PAH size and charge, with the F300M and F360M allowing for robust continuum subtraction for F335M to isolate the 3.3 μm PAH feature. The F1000W and F2100W capture the dust continuum, with a
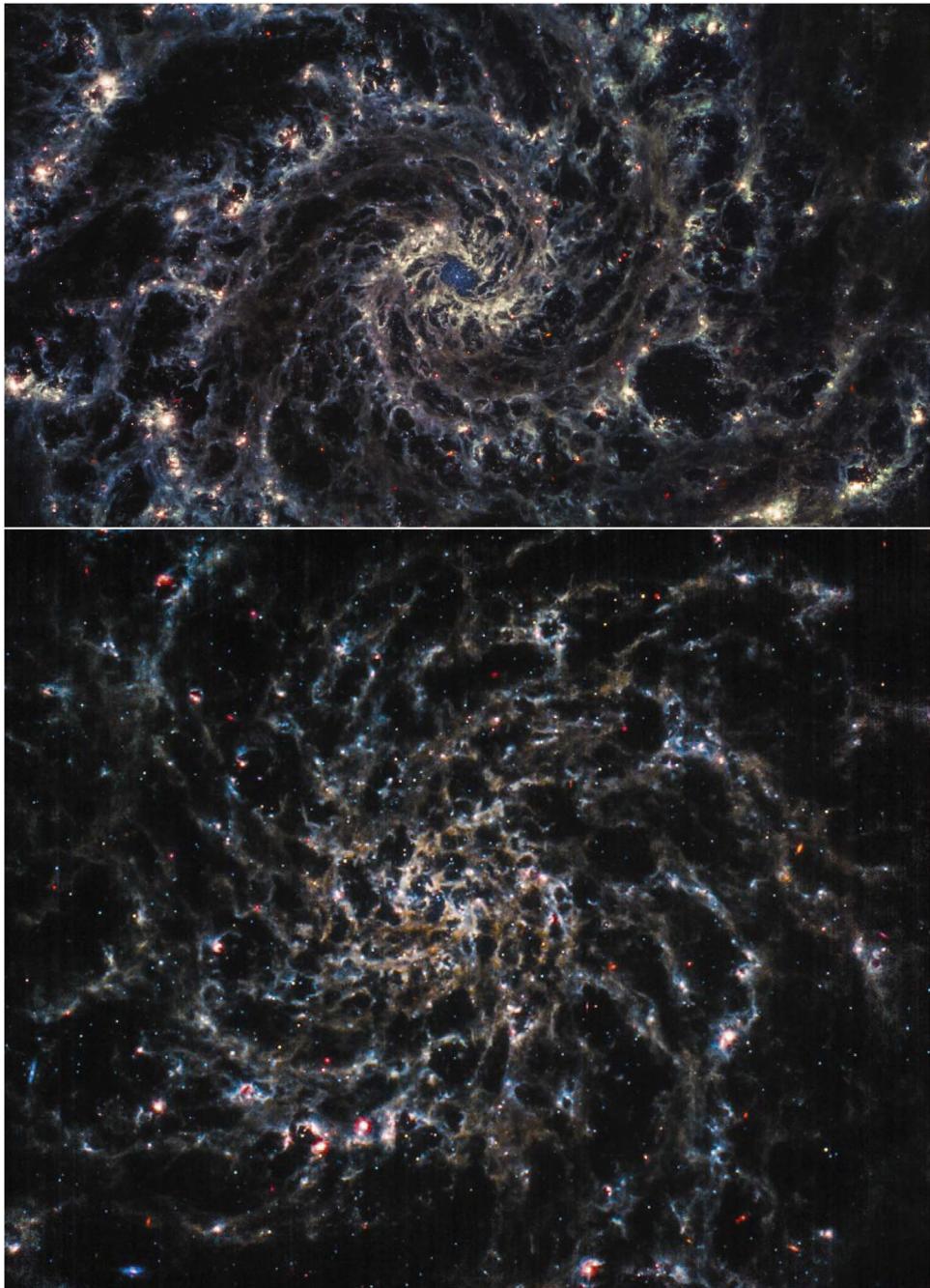
Figure 7. Color-composite images produced by J. Schmidt from MIRI data of NGC 628 (top) and IC 5332 (bottom). Red: MIRI F2100W; orange: MIRI F1130W; cyan: MIRI F770W; extra overall brightness in grayscale: MIRI F1000W. The images were used as the models for the first two ESA/JWST Pictures of the Month from the JWST Cycle 1 General Observers Program as featured at https://esawebb.org/images/potm2208a/ and https://esawebb.org/images/comparisons/potm2209a/.

possible contribution to the F1000W band by silicate absorption.

Together with data from HST, MUSE, and ALMA, the integrated PHANGS data set allows for multiscale, multiphase studies of the star formation cycle across a range of galactic environments. In Figure 2, the five UV-optical filters used in the PHANGS–HST program (Lee et al. 2022) are also shown; these mainly sample the stellar continuum and provide a view of dust in extinction. The HST imaging provides high angular resolution ($0''.8$), comparable to JWST NIRCam imaging at $2\,\mu$m. The PHANGS–MUSE program (Emsellem et al. 2022) provides integral field unit spectroscopy over $0.475 < \lambda/$ μm < 0.935, covering many of the same bands as HST but with coarser angular resolution ($\sim 1''$). PHANGS–ALMA (Leroy et al. 2021) shows the distribution and kinematics of the CO that traces the star-forming molecular medium, also at $\sim 1''$ resolution.

6.1. Constraining the Natal Cluster Mass Function and Cluster Formation Efficiency

PHANGS–JWST near- and mid-IR imaging will be used to detect dust-embedded clusters and associations, mitigate and measure the effects of extinction, and constrain other physical

Figure 8. Same as Figure 7 but for NGC 1365 (top) and NGC 7496 (bottom).

properties such as age and mass through SED fitting (e.g., Figure 9). We will test different selection strategies to systematically identify embedded cluster candidates and produce the first complete catalogs of these sites of the earliest stages of star formation. The catalogs will enable us to measure the fraction of stars that are born in compact clusters, characterize the distribution of cluster masses at birth, and investigate dependence on environment.

The ensemble properties of star clusters are highly debated in the literature (e.g., Larsen 2009; Chandar et al. 2017; Krumholz et al. 2019; Adamo et al. 2020a, 2020b). Due to dust extinction, it has been difficult to obtain a truly complete census of clusters across all galactic environments and ages. The PHANGS–JWST infrared imaging will now allow us to study the clusters in dusty galaxy centers, spiral arms, and bar-end regions. These are sites where super star clusters tend to be found, the cluster formation efficiency is expected to be highest (e.g., Kruijssen 2012; Krumholz 2014; Adamo et al. 2015; Ginsburg & Kruijssen 2018; Grudić et al. 2021), and molecular cloud populations show clear enhancements in both density and turbulence (e.g., Longmore et al. 2014; Beuther et al. 2017; Sun et al. 2020; Henshaw et al. 2022). Extrapolating from the
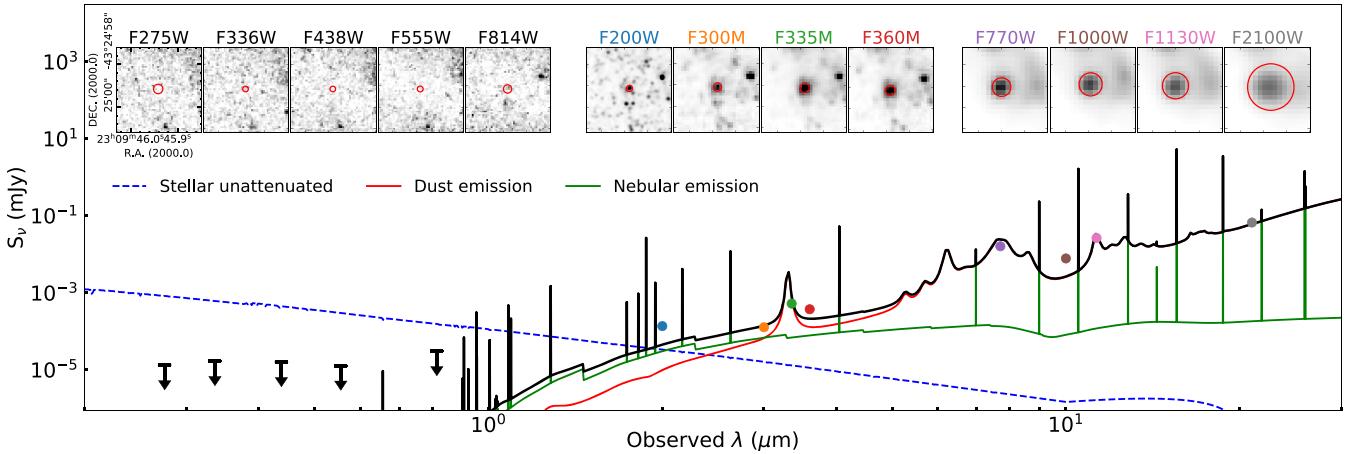
Figure 9. Example of a dust-embedded young star cluster, a compact infrared source with no detection in the optical HST images. Postage stamps from all 13 HST +JWST PHANGS images are shown together with photometry as an illustration of the SED fitting that will be performed in the future to constrain the physical properties of these objects.

visible cluster population, we expect to detect $\gtrsim$100 new embedded clusters in each galaxy, or $\sim$2000 across the sample, with the greatest gain in the dustiest and most active parts of the sample. Analysis combining JWST with HST data will also allow us to break the age-reddening degeneracy for optically detected clusters and derive robust constraints on age, mass, and reddening for both embedded and visible cluster populations (e.g., Figure 2).

These investigations use the full set of PHANGS–JWST data for measuring the properties of embedded clusters. In particular, the near-IR bands provide key constraints on stellar properties. The F200W observations provide good visibility through the dust in the region of the SED still dominated by stellar photospheric emission. The excellent angular resolution (0.″07) at 2 μm is required to resolve star clusters, which have effective radii between 0.5 and about 10 pc (Portegies Zwart et al. 2010; Ryon et al. 2017).

Rodriguez et al. (2023) and Whitmore et al. (2023b) took the first steps in identifying embedded clusters, estimating their physical properties, and examining the incompleteness in optical samples. Hoyer et al. (2023) studied the nuclear star cluster in NGC 628 and the nature of the mid-infrared structure surrounding it. Schinnerer et al. (2023) showed that massive, dusty clusters can provide a sensitive diagnostic of the very dusty star-forming environments in nuclear regions when comparing ALMA data and simulations. Some of the clusters detected in the PHANGS–JWST survey push current stellar and dust models used by CIGALE to their limits due to their very young ages, high dust content, and/or low mass. Including dust models computed in the optically thick case and stellar populations with a stochastically sampled initial mass function may prove necessary to model such clusters.

6.2. Measuring the Duration of Embedded Star Formation

PHANGS–JWST data enable characterization of the poorly studied embedded phase of star formation before feedback disrupts the natal cloud. Observations that resolve galaxies into discrete star-forming regions, clusters, and molecular clouds have enabled statistical measurements of the timescales associated with the major phases of the star formation cycle (e.g., Kawamura et al. 2009; Kruijssen & Longmore 2014; Meidt et al. 2015; Corbelli et al. 2017; Grasha et al. 2018;

Kruijssen et al. 2018, 2019a; Grasha et al. 2019; Hannon et al. 2019, 2022; Chevance et al. 2020a; Kim et al. 2022; Ward et al. 2022). Over the last decade, the (anti)correlation between clouds and H II regions or optically identified clusters has constrained the total lifetimes of clouds to 10–30 Myr (where the range represents the physical variation rather than the uncertainty; see, e.g., Chevance et al. 2020b, 2022a). However, both the duration of the earliest, embedded phase and the length of time that a cloud remains truly devoid of star formation activity remain poorly known.

Measuring these timescales is essential for understanding the dominant physics of star formation. The time between cloud formation and the onset of star formation constrains the (im) balance between the driving and decay of turbulence (e.g., Gnedin et al. 2016; Padoan et al. 2017). The duration of the embedded phase reflects the time that it takes feedback to start dispersing a cloud (e.g., Olivier et al. 2021). Measuring the embedded timescale can also distinguish between models in which star and cluster formation "accelerate" over a cloud's lifetime (Murray 2011; Lee et al. 2016) and those that favor a more steady process (Krumholz & McKee 2005; Krumholz & Tan 2007; Krumholz & McKee 2020). Timescales for the embedded and optically visible stages can be used to infer which feedback mechanisms quench star formation (e.g., Lopez et al. 2014; Kruijssen et al. 2019a; Kim et al. 2022; Chevance et al. 2022b; Hannon et al. 2022) and whether clouds are magnetically sub- or supercritical (Kim et al. 2021b).

Accessing the embedded phase of star formation requires a tracer of obscured star formation that reaches the scale of individual clouds. The limited resolution of Spitzer ($\sim$6″) limited the number of galaxies where such measurements were possible to five (Kim et al. 2021a). With the increased spatial resolution and sensitivity in the mid-infrared achieved with MIRI, the time evolution of the early stages of star formation can now be characterized in galaxies out to $\sim$30 Mpc.

By combining some of the first PHANGS–JWST MIRI observations with PHANGS–ALMA CO observations (Leroy et al. 2021), Kim et al. (2023) determined the relative duration of the early phases of star formation, from truly quiescent clouds, to embedded star formation, revealed star formation, and cold gas-free H II regions in NGC 628. In combination with the stellar "clocks" offered by star clusters (see Section 6.1) and Hα emission (e.g., Leroy et al. 2013; Haydon et al. 2020), these

relative measurements are converted into absolute timescales. PHANGS–JWST data will enable this measurement across the wide range of environments that are present in the sample. These observations will constrain how the physical mechanisms that regulate and drive the successive phases of star formation map to the environment.

6.3. Characterizing How Dust Properties Respond to the Local Environment

Most of the imaging bands used in PHANGS–JWST show emission features from dust continuum and PAHs. The PAHs reprocess as much as 20% of all absorbed stellar UV/optical light (Smith et al. 2007). As they do so, they eject electrons that heat the ISM and produce bright mid-IR emission features (e.g., Tielens 2008) that are among the most highly detectable star formation tracers across cosmic time (e.g., Riechers et al. 2014). However, PAH properties and abundance vary substantially within and between galaxies. Fewer PAHs are present in H II regions or at low metallicities (e.g., Engelbracht et al. 2005; Chastenet et al. 2019), but they can make up >5% of the dust mass in the diffuse ISM of solar metallicity galaxies (Draine et al. 2007; Aniano et al. 2020). This variability hampers the use of PAH emission as a star formation tracer (Calzetti et al. 2007; Whitcomb et al. 2020) and leads to critical uncertainties when modeling their role in the ISM. The PHANGS–JWST Treasury data will yield the first highly resolved atlas of PAH properties—abundance, size distribution, and charge inferred from mid-IR band ratios—in the nearby galaxy population. These data can be used to build an empirical model to predict the abundance and characteristics of PAHs as a function of local metallicity, ISM phase, density, and radiation field (from HST, MUSE, and ALMA). The measurements underpinning this model must be highly resolved because radiation field, density, and ISM phase can vary by factors of $\sim$1000 on 10–100 pc scales, altering the PAHs (Chastenet et al. 2019; Draine et al. 2021). The PHANGS–JWST first results in this Issue from Chastenet et al. (2023a, 2023b), Dale et al. (2023), and Egorov et al. (2023) all show that PAH emission properties do indeed vary systematically with the local galactic environment.

6.4. A High-resolution View of the Neutral ISM

The PAH emission offers a promising tracer for the structure of the neutral ISM. Traditionally, H I 21 cm emission and the lowest-energy rotational lines of CO ($\lambda = 2.6$ and 1.3 mm) have been used to map out the atomic and molecular phases of the ISM. These tracers suffer some limitations; the very long wavelength of 21 cm emission makes it intrinsically faint, and current interferometers can typically only achieve resolutions of $5''$–$10''$ for nonprohibitive integration times. The (sub) millimeter CO emission lines are at shorter wavelengths, and thus a significantly better resolution of $1''$ can be achieved with ALMA (Leroy et al. 2021), but they are an imperfect proxy for the H_2 that constitutes the molecular ISM. With JWST, the mid-IR PAH emission potentially provides a much higher-resolution view ($<0''.37$) of the same interstellar gas that is traced by H I and CO. While the emissivity of PAHs likely varies with environment (Draine et al. 2007; Hensley & Draine 2022), the spatial distribution of the mid-IR PAH emission yields an exceptionally detailed, high dynamic range image of the structure of neutral gas in a galaxy. Based on

studies in the Milky Way and the nearest galaxies, the older "spherical cloud" view of the ISM has been integrated with a newer filamentary description of ISM structure (Hacar et al. 2022). The enthusiasm for such a filamentary view has been driven by infrared imaging by the previous generations of instruments, but it was difficult to extend this view to a galactic scale in all but the nearest galaxies. The JWST imaging of PAH emission yields such high-resolution maps of neutral gas throughout the Local Volume.

Figure 7 shows the filamentary organization of the gas in NGC 628, which prompted initial investigations of ISM structure using PAHs as ISM tracers (e.g., Sandstrom et al. 2023b; Barnes et al. 2023; Watkins et al. 2023). Sandstrom et al. (2023b) demonstrated a new JWST band combination that produces high-quality maps of the PAH feature at 3.3 μm with excellent stellar continuum subtraction. These maps offer the highest-resolution ($0''.11$) wide-area maps of the ISM in nearby galaxies. Sandstrom et al. (2023b) verified that PAH features are intimately connected to the neutral ISM and used the genus statistic for characterizing the emission topology. Thilker et al. (2023) showed how the filamentary network of 3.3 μm PAH emission relates to extinction lanes identified in the optical HST imaging and to the young cluster population of a galaxy. Meidt et al. (2023) showed that the spatial separation scales between filaments is consistent with large-scale gravitational fragmentation models. Williams et al. (2022) leveraged the high-resolution images to make a careful measurement of evolutionary timescales in a spiral arm spur.

The PAH imaging also shows us where the neutral ISM is *not* found. Rings of PAH emission with faint centers can be used to define the wall of "bubbles" or feedback-driven shells. While bubbles from feedback have been long studied (e.g., Oey & Clarke 1997; Weisz et al. 2009, and references therein), the exquisite resolution, sensitivity to structure on many scales, and wide dynamic range of the PHANGS–JWST images make them an excellent tracer of bubble walls. PHANGS–JWST data can be used to produce inventories of bubbles and shell features. These structures can be connected to the sources of feedback identified from PHANGS–MUSE and PHANGS–HST catalogs of star clusters and associations and to the kinematics of the cold ISM as traced by PHANGS–ALMA. As an early demonstration of such analyses, Watkins et al. (2023) created a bubble catalog for NGC 628 and examined the properties, including the size distribution for the ensemble population. Barnes et al. (2023) demonstrated the capabilities of the PHANGS multiwavelength data set for measuring the expansion rates and understanding the origins of large kiloparsec-scale cavities, focusing on the "Phantom Void" in the southeast quadrant of NGC 628.

6.5. Robust Mid-IR Star Formation Diagnostics from Cloud to Galaxy Scales

Mid-IR emission from hot dust is widely used to trace star formation at both low and high z (e.g., Kennicutt & Evans 2012). Unfortunately, the calibration of mid-IR star formation tracers has a strong dependence on both spatial scale and environment (e.g., Boquien et al. 2015), which likely stems from a variable heating contribution by old stars and uncertain dust geometry (e.g., Groves et al. 2012; Nersesian et al. 2019). PHANGS–JWST imaging, combined with supporting PHANGS data sets, enables a data-driven description of the origin and variations in mid-IR emission. Mid-IR emission is

due to the heating of dust and PAHs by both young and old stars, but the bright thermal dust emission in the mid-IR continuum bands (F2100W and F1000W) is expected to respond differently to the local dust-heating radiation field than the PAH emission (Draine et al. 2007; Hensley & Draine 2022), offering a potentially powerful diagnostic of local interstellar conditions. With the insights obtained by comparing mid-IR band ratios and physical dust models, we will build on previous work that calibrated the mid-IR emission as an SFR indicator on galaxy-wide and subkiloparsec scales (e.g., Calzetti et al. 2007).

Combining robust high-resolution measurements of the embedded star formation from PHANGS–JWST with PHANGS–ALMA and PHANGS–MUSE imaging of the molecular gas and optically visible tracers of star formation and feedback will enable the first cloud-scale inventory of all stages in the star formation cycle across the 19 galaxies in our sample. Previous work on $\lesssim 100$ pc scales suggested that up to $\sim 60\%$ of molecular gas in galaxies may be devoid of Hα emission (e.g., Onodera et al. 2010; Schruba et al. 2010; Kreckel et al. 2018; Kruijssen et al. 2019a; Schinnerer et al. 2019b; Chevance et al. 2020a; Kim et al. 2022; Pan et al. 2022). Yet highly resolved IR observations show that truly non-star-forming clouds are scarce in our galaxy (Mooney & Solomon 1988; Ginsburg et al. 2012), and Spitzer results suggest that molecular clouds in Local Group galaxies spend up to half their lifetime hosting only embedded massive star formation (Kim et al. 2021a). With PHANGS–JWST, we will confirm whether there is a large reservoir of molecular gas without star formation in nearby star-forming disk galaxies and, if so, whether it is due to a delayed onset (e.g., Gnedin et al. 2016; Padoan et al. 2017) or sustained suppression (e.g., Federrath et al. 2016; Semenov et al. 2017; Meidt et al. 2018, 2020; Kruijssen et al. 2019b) of star formation.

PHANGS–JWST high-resolution measurements will also enable important empirical tests of cloud-scale models of star formation. These models predict the integrated and per freefall time SFR and efficiency of individual clouds based on their density, turbulence, and dynamical state (e.g., Padoan et al. 2017; Kim et al. 2021b), quantities that have already been measured using the PHANGS–ALMA data (e.g., Sun et al. 2020, 2022). Cloud-scale star formation models are widely used to interpret observations (e.g., Barnes et al. 2017; Utomo et al. 2018) and implemented as subgrid models in galaxy simulations (e.g., Gensior et al. 2020; Kretschmer & Teyssier 2020). The models have never been rigorously tested beyond the Local Group, however, since the rapid action of feedback prohibits linking optical SFR estimates to the progenitor cloud's gas mass and hence the integrated SFR per unit gas mass. Lacking cloud-by-cloud estimates of the embedded star formation activity, studies in external galaxies have resorted to using population averages, obtaining results that suggest—but cannot currently prove—important inconsistencies with the models, such as inferred star formation efficiencies that decrease with the gravitational boundedness of the gas (e.g., Leroy et al. 2017; Schruba et al. 2019). The new PHANGS–JWST data are essential for unambiguous cloud-scale tests of these predictions.

The PHANGS–JWST papers in this Issue have begun to explore these questions. Hassani et al. (2023) studied compact sources in F2100W, finding that nearly all sources are compact star-forming regions. These regions show strong associations with both the molecular gas and Hα emission. Liu et al. (2023) evaluated how strong heating in the IR from dusty star-forming regions is connected to the density and temperature of the molecular ISM as seen by ALMA. Leroy et al. (2023) used a large set of archival data to show that the mid-IR has an excellent capacity to trace the properties of the star-forming ISM. This retrospective analysis provides context for the high-resolution view provided by PHANGS–JWST. Using the new data, Leroy et al. (2023) conducted a correlation analysis of the mid-IR data, showing strong correlations with both the Hα and the CO in galaxies, and these correlations are stronger than the correlation between Hα and CO at high resolution.

7. Data Products

Preliminary JWST image products for NGC 7496, IC 5332, NGC 628, and NGC 1365, used as the basis for the PHANGS–JWST first results presented in this volume, are available at the Canadian Astronomy Data Centre (CADC) as part of the PHANGS archive.[79] This data release includes stacked, mosaicked, calibrated images based on all PHANGS–JWST data obtained through 2022 August: imaging in four NIRCam and four MIRI filters for NGC 7496, NGC 628, and NGC 1365 and in four MIRI filters for IC 5332.[80] The processing of these data is subject to the caveats discussed in Section 4.8.

After the completion of the PHANGS–JWST observations, we will provide an expanded set of image products for all 19 galaxies through MAST, as well as at the CADC PHANGS archive. We anticipate significant improvements in the processing and calibration to address currently known issues (Sections 4 and 4.8), as well as those that arise in future analyses. These later data releases will include the full PHANGS–JWST imaging stack at native resolution together with products convolved to match the angular resolution of the lowest-resolution PHANGS–JWST image (MIRI 21 μm) and other PHANGS data sets (e.g., maps from ALMA and MUSE).

The PHANGS–JWST papers in this Issue give examples of the high-level science products that would be valuable to develop from JWST data in combination with the rest of the PHANGS surveys.

The PHANGS–JWST first results on stellar clusters illustrate the potential (and challenges) in using the data at their highest resolution (which at 2 μm surpasses the resolution of HST optical imaging) to develop catalogs of embedded star clusters, augment the PHANGS–HST star cluster and association catalogs[81] with photometry from 2 to 21 μm, and measure their physical properties through SED fitting (Whitmore et al. 2023b; Hoyer et al. 2023; Rodriguez et al. 2023). Catalogs of compact sources in the MIRI bands can be produced to identify larger star-forming regions on scales comparable to the H II regions observed with MUSE and the giant molecular clouds resolved by ALMA (Hassani et al. 2023; Schinnerer et al. 2023). As PHANGS–JWST analysis matures, it will be possible to develop complete catalogs of dust-enshrouded and visible stellar populations across multiple physics scales (Larson et al. 2022), which include physical properties such as mass, age, and dust reddening, via SED fitting, which is able

---

[79] CANFAR PHANGS–JWST Treasury Survey Data publication: doi:10.11570/22.0082.
[80] See also footnote 70.
[81] HST catalogs available on MAST: doi:10.17909/jray-9798.

to break degeneracies between reddening and age (Whitmore et al. 2023a).

The PHANGS–JWST first results on feedback show how catalogs of ISM bubbles and shells can be produced (Barnes et al. 2023; Watkins et al. 2023) and used in combination with catalogs of the young stellar populations to identify the contribution of feedback and dynamical processes in the formation and evolution of these structures. The importance of complete inventories of the youngest stellar populations and feedback-driven ISM structures and of access to the earliest embedded phase of star formation via mid-IR JWST imaging for quantitative estimates of timescales, star formation efficiencies, and feedback parameters is also highlighted by Kim et al. (2023), Watkins et al. (2023), and Barnes et al. (2023).

As shown in Section 5, JWST's high-resolution capabilities have provided the most detailed maps of the diffuse ISM possible in nearby galaxies to date to enable studies of local influences on heating (Leroy et al. 2023). Dust emission and absorption maps can be produced from the combination of the PHANGS–JWST, HST, VLT-MUSE, and ALMA data sets (e.g., Meidt et al. 2023; Thilker et al. 2023; Williams et al. 2022).

Finally, the PHANGS–JWST first results show how PAH features can be sensitive diagnostics of ISM conditions through changing flux ratios. Using empirical methods, Sandstrom et al. (2023a) demonstrated how to isolate PAH features from the stellar continuum using JWST bands, which can be developed into a full set of PAH-only maps of the galaxies. Chastenet et al. (2023a, 2023b) used JWST data to find variation in PAH properties in the broader ISM, with Egorov et al. (2023) and Dale et al. (2023) exploring H II regions and star clusters, respectively. These ratio measurements can be refined into environmental diagnostics of properties like the metallicity and radiation field.

8. Summary

We present the PHANGS–JWST Cycle 1 Treasury program, one of the key observational campaigns conducted by the PHANGS collaboration (Schinnerer et al. 2019a). PHANGS–JWST is a 112.6 hr program to image 19 nearby galaxies ($D < 20$ Mpc) in eight filters from 2 to 21 μm using NIRCam (F200W, F300M, F335M, and F360M) and MIRI (F770W, F1000W, F1130W, and F2100W).

1. We summarize the properties of the PHANGS–JWST nearby spiral galaxy sample, which all have overlapping coverage from ALMA, HST, VLT-MUSE, and other facilities (Section 2), and present our NIRCam and MIRI observing strategy (Section 3).

2. In Section 4, we present the modifications to the standard pipeline and additional processing steps used to produce the data products for the first results analysis in this Issue. In particular, we describe changes to the default astrometric alignment, a mitigation strategy for the $1/f$ noise in NIRCam using PCA, and a background validation strategy for MIRI data. Current limitations and uncertainties in this first reduction are summarized.

3. In Section 5, we provide an overview of the imaging of the first four targets (NGC 0628, NGC 1365, NGC 7496, and IC 5332), compare our new JWST data to existing Spitzer imaging, and compute limiting point-source and

surface brightness sensitivities of the data. We highlight the value of the PHANGS–JWST imaging for engaging the public in JWST discovery.

4. In Section 6, we describe the science goals of our program and preview the letters in this Issue, while in Section 7, we describe the currently available and planned future image products, as well as higher-level science products that would be valuable to develop for the community.

As a public Cycle 1 Treasury program, the PHANGS–JWST data set is designed to broadly enable community science beyond the team science objectives outlined here. Open access to such standard imaging observations early in the mission is essential for learning how to best study star formation, stellar populations, and dust in the local universe at high resolution in the infrared with JWST. The early publication of our first results, initial lessons learned with data processing, and challenges to be addressed as we expand analysis to the full PHANGS–JWST sample are intended to serve as a pathfinder to facilitate forthcoming work.

ORCID iDs

Janice C. Lee ● https://orcid.org/0000-0002-2278-9407
Karin M. Sandstrom ● https://orcid.org/0000-0002-4378-8534
Adam K. Leroy ● https://orcid.org/0000-0002-2545-1700
David A. Thilker ● https://orcid.org/0000-0002-8528-7340
Eva Schinnerer ● https://orcid.org/0000-0002-3933-7677
Erik Rosolowsky ● https://orcid.org/0000-0002-5204-2259
Kirsten L. Larson ● https://orcid.org/0000-0003-3917-6460
Oleg V. Egorov ● https://orcid.org/0000-0002-4755-118X
Thomas G. Williams ● https://orcid.org/0000-0002-0012-2142

Judy Schmidt ● https://orcid.org/0000-0002-2617-5517
Eric Emsellem ● https://orcid.org/0000-0002-6155-7166
Gagandeep S. Anand ● https://orcid.org/0000-0002-5259-2314
Ashley T. Barnes ● https://orcid.org/0000-0003-0410-4504
Francesco Belfiore ● https://orcid.org/0000-0002-2545-5752
Ivana Bešlić ● https://orcid.org/0000-0003-0583-7363
Frank Bigiel ● https://orcid.org/0000-0003-0166-9745
Guillermo A. Blanc ● https://orcid.org/0000-0003-4218-3944
Alberto D. Bolatto ● https://orcid.org/0000-0002-5480-5686
Médéric Boquien ● https://orcid.org/0000-0003-0946-6176
Jakob den Brok ● https://orcid.org/0000-0002-8760-6157
Yixian Cao ● https://orcid.org/0000-0001-5301-1326
Rupali Chandar ● https://orcid.org/0000-0003-0085-4623
Jérémy Chastenet ● https://orcid.org/0000-0002-5235-5589
Mélanie Chevance ● https://orcid.org/0000-0002-5635-5180
I-Da Chiang (江宜達) ● https://orcid.org/0000-0003-2551-7148
Enrico Congiu ● https://orcid.org/0000-0002-8549-4083
Daniel A. Dale ● https://orcid.org/0000-0002-5782-9093
Sinan Deger ● https://orcid.org/0000-0003-1943-723X
Cosima Eibensteiner ● https://orcid.org/0000-0002-1185-2810
Christopher M. Faesi ● https://orcid.org/0000-0001-5310-467X
Simon C. O. Glover ● https://orcid.org/0000-0001-6708-1317
Kathryn Grasha ● https://orcid.org/0000-0002-3247-5321
Brent Groves ● https://orcid.org/0000-0002-9768-0246
Hamid Hassani ● https://orcid.org/0000-0002-8806-6308
Kiana F. Henny ● https://orcid.org/0000-0001-7448-1749
Jonathan D. Henshaw ● https://orcid.org/0000-0001-9656-7682
Nils Hoyer ● https://orcid.org/0000-0001-8040-4088
Annie Hughes ● https://orcid.org/0000-0002-9181-1161
Sarah Jeffreson ● https://orcid.org/0000-0002-4232-0200
María J. Jiménez-Donaire ● https://orcid.org/0000-0002-9165-8080
Jaeyeon Kim ● https://orcid.org/0000-0002-0432-6847
Hwihyun Kim ● https://orcid.org/0000-0003-4770-688X
Ralf S. Klessen ● https://orcid.org/0000-0002-0560-3172
Eric W. Koch ● https://orcid.org/0000-0001-9605-780X
Kathryn Kreckel ● https://orcid.org/0000-0001-6551-3091
J. M. Diederik Kruijssen ● https://orcid.org/0000-0002-8804-0212
Jing Li ● https://orcid.org/0000-0002-4825-9367
Daizhong Liu ● https://orcid.org/0000-0001-9773-7479
Laura A. Lopez ● https://orcid.org/0000-0002-1790-3148
Daniel Maschmann ● https://orcid.org/0000-0001-6038-9511
Ness Mayker Chen ● https://orcid.org/0000-0002-5993-6685
Sharon E. Meidt ● https://orcid.org/0000-0002-6118-4048
Eric J. Murphy ● https://orcid.org/0000-0001-7089-7325
Justus Neumann ● https://orcid.org/0000-0002-3289-8914
Nadine Neumayer ● https://orcid.org/0000-0002-6922-2598
Hsi-An Pan ● https://orcid.org/0000-0002-1370-6964
Ismael Pessa ● https://orcid.org/0000-0002-0873-5744
Jérôme Pety ● https://orcid.org/0000-0003-3061-6546
Miguel Querejeta ● https://orcid.org/0000-0002-0472-1011
Francesca Pinna ● https://orcid.org/0000-0001-5965-3530
M. Jimena Rodríguez ● https://orcid.org/0000-0002-0579-6613
Toshiki Saito ● https://orcid.org/0000-0001-9016-2641
Patricia Sánchez-Blázquez ● https://orcid.org/0000-0003-0651-0098
Francesco Santoro ● https://orcid.org/0000-0002-6363-9851
Amy Sardone ● https://orcid.org/0000-0002-5783-145X
Rowan J. Smith ● https://orcid.org/0000-0002-0820-1814
Mattia C. Sormani ● https://orcid.org/0000-0001-6113-6241
Fabian Scheuermann ● https://orcid.org/0000-0003-2707-4678
Sophia K. Stuber ● https://orcid.org/0000-0002-9333-387X
Jessica Sutter ● https://orcid.org/0000-0002-9183-8102
Jiayi Sun (孙嘉懿) ● https://orcid.org/0000-0003-0378-4667
Yu-Hsuan Teng ● https://orcid.org/0000-0003-4209-1599

Robin G. Treß ⓘ https://orcid.org/0000-0002-9483-7164
Antonio Usero ⓘ https://orcid.org/0000-0003-1242-505X
Elizabeth J. Watkins ⓘ https://orcid.org/0000-0002-7365-5791
Bradley C. Whitmore ⓘ https://orcid.org/0000-0002-3784-7032
Alessandro Razza ⓘ https://orcid.org/0000-0001-7876-1713

References

Adamo, A., Kruijssen, J. M. D., Bastian, N., Silva-Villa, E., & Ryon, J. 2015, MNRAS, 452, 246

Adamo, A., Hollyhead, K., Messa, M., et al. 2020a, MNRAS, 499, 3267

Adamo, A., Zeidler, P., Kruijssen, J. M. D., et al. 2020b, SSRv, 216, 69

Anand, G. S., Lee, J. C., Van Dyk, S. D., et al. 2021a, MNRAS, 501, 3621

Anand, G. S., Rizzi, L., Tully, R. B., et al. 2021b, AJ, 162, 80

Aniano, G., Draine, B. T., Gordon, K. D., & Sandstrom, K. 2011, PASP, 123, 1218

Aniano, G., Draine, B. T., Hunt, L. K., et al. 2020, ApJ, 889, 150

Armus, L., Mazzarella, J. M., Evans, A. S., et al. 2009, PASP, 121, 559

Astropy Collaboration, Price-Whelan, A. M., Sipőcz, B. M., et al. 2018, AJ, 156, 123

Astropy Collaboration, Price-Whelan, A. M., Lim, P. L., et al. 2022, ApJ, 935, 167

Barnes, A., Watkins, E. J., Meidt, S. E., et al. 2023, ApJL, 944, L22

Barnes, A. T., Longmore, S. N., Battersby, C., et al. 2017, MNRAS, 469, 2263

Becklin, E. E., & Neugebauer, G. 1967, ApJ, 147, 799

Beuther, H., Meidt, S., Schinnerer, E., Paladino, R., & Leroy, A. 2017, A&A, 597, A85

Boquien, M., Burgarella, D., Roehlly, Y., et al. 2019, A&A, 622, A103

Boquien, M., Calzetti, D., Aalto, S., et al. 2015, A&A, 578, A8

Boyer, M. L., Anderson, J., Gennaro, M., et al. 2022, RNAAS, 6, 191

Brinchmann, J., Charlot, S., White, S. D. M., et al. 2004, MNRAS, 351, 1151

Budavári, T., Wild, V., Szalay, A. S., Dobos, L., & Yip, C.-W. 2009, MNRAS, 394, 1496

Buta, R. J., Sheth, K., Athanassoula, E., et al. 2015, ApJS, 217, 32

Butterworth, S. 1930, Experimental Wireless & the Wireless Engineer, 7, 536

Calzetti, D., Kennicutt, R. C., Engelbracht, C. W., et al. 2007, ApJ, 666, 870

Chandar, R., Michael Fall, S., Whitmore, B. C., & Mulia, A. J. 2017, ApJ, 849, 128

Chastenet, J., Sandstrom, K., Chiang, I.-D., et al. 2019, ApJ, 876, 62

Chastenet, J., Sutter, J., Sandstrom, K. M., et al. 2023a, ApJL, 944, L12

Chastenet, J., Sutter, J., Sandstrom, K. M., et al. 2023b, ApJL, 944, L11

Chevance, M., Krumholz, M. R., McLeod, A. F., et al. 2022a, arXiv:2203.09570

Chevance, M., Kruijssen, J. M. D., Hygate, A. P. S., et al. 2020, MNRAS, 493, 2872

Chevance, M., Kruijssen, J. M. D., Vazquez-Semadeni, E., et al. 2020b, SSRv, 216, 50

Chevance, M., Kruijssen, J. M. D., Krumholz, M. R., et al. 2022b, MNRAS, 509, 272

Corbelli, E., Braine, J., Bandiera, R., et al. 2017, A&A, 601, A146

Dale, D., Boquien, M., Barnes, A., et al. 2023, ApJL, 944, L23

Dale, D. A., Bendo, G. J., Engelbracht, C. W., et al. 2005, ApJ, 633, 857

Dale, D. A., Cohen, S. A., Johnson, L. C., et al. 2009, ApJ, 703, 517

de Vaucouleurs, G., de Vaucouleurs, A., Corwin, H. G., Jr., et al. 1991, Third Reference Catalogue of Bright Galaxies. Volume I: Explanations and references. Volume II: Data for galaxies between 0ʰ and 12ʰ. Volume III: Data for galaxies between 12ʰ and 24ʰ (New York: Springer))

Deger, S., Lee, J. C., Whitmore, B. C., et al. 2022, MNRAS, 510, 32

Dolphin, A. 2016, DOLPHOT: Stellar Photometry, Astrophysics Source Code Library, ascl:1608.013

Draine, B. T., Li, A., Hensley, B. S., et al. 2021, ApJ, 917, 3

Draine, B. T., Dale, D. A., Bendo, G., et al. 2007, ApJ, 663, 866

Egorov, O., Kreckel, K., Sandstrom, K. M, et al. 2023, ApJL, 944, L16

Emsellem, E., Schinnerer, E., Santoro, F., et al. 2022, A&A, 659, A191

Engelbracht, C. W., Gordon, K. D., Rieke, G. H., et al. 2005, ApJL, 628, L29

Federrath, C., Rathborne, J. M., Longmore, S. N., et al. 2016, ApJ, 832, 143

Freedman, W. L., Madore, B. F., Gibson, B. K., et al. 2001, ApJ, 553, 47

Gaia Collaboration, Prusti, T., de Bruijne, J. H. J., et al. 2016, A&A, 595, A1

Gensior, J., Kruijssen, J. M. D., & Keller, B. W. 2020, MNRAS, 495, 199

Ginsburg, A., Bressert, E., Bally, J., & Battersby, C. 2012, ApJL, 758, L29

Ginsburg, A., & Kruijssen, J. M. D. 2018, ApJL, 864, L17

Gnedin, N. Y., et al. 2016, Star Formation in Galaxy Evolution: Connecting Numerical Models to Reality, Saas-Fee Advanced Course, Vol. 43 (Berlin: Springer), 85

Grasha, K., Calzetti, D., Bittle, L., et al. 2018, MNRAS, 481, 1016

Grasha, K., Calzetti, D., Adamo, A., et al. 2019, MNRAS, 483, 4707

Groves, B., Krause, O., Sandstrom, K., et al. 2012, MNRAS, 426, 892

Groves, B., Kreckel, K., Santoro, F., et al. 2023, MNRAS, Advance Access

Grudić, M. Y., Kruijssen, J. M. D., Faucher-Giguère, C.-A., et al. 2021, MNRAS, 506, 3239

Hacar, A., Clark, S., Heitsch, F., et al. 2022, arXiv:2203.09562

Hannon, S., Lee, J. C., Whitmore, B. C., et al. 2019, MNRAS, 490, 4648

Hannon, S., Lee, J. C., Whitmore, B. C., et al. 2022, MNRAS, 512, 1294

Hassani, H., Rosolowsky, E. W., Leroy, A. K., et al. 2023, ApJL, 944, L21

Haydon, D. T., Kruijssen, J. M. D., Chevance, M., et al. 2020, MNRAS, 498, 235

Henshaw, J. D., Barnes, A. T., Battersby, C., et al. 2022, arXiv:2203.11223

Hensley, B. S., & Draine, B. T. 2022, arXiv:2208.12365

Hoyer, N., Pinna, F., Kamlah, A. W. H., et al. 2023, ApJL, 944, L25

Joye, W. A., & Mandel, E. 2003, in ASP Conf. Ser. 295, Astronomical Data Analysis Software and Systems XII, ed. H. E. Payne, R. I. Jedrzejewski, & R. N. Hook (San Francisco: ASP), 489

Kawamura, A., Mizuno, Y., Minamidani, T., et al. 2009, ApJS, 184, 1

Kennicutt, R. C., & Evans, N. J. 2012, ARA&A, 50, 531

Kennicutt, R., Jr., Armus, L., Bendo, G., et al. 2003, PASP, 115, 928

Kessler, M. F., Mueller, T. G., Leech, K., et al. 2003, in The ISO Handbook, Volume I—Mission and Satellite Overview, ed. T. G. Mueller, J. A. D. L. Blommaert, & P. Garcia-Lario (Paris: European Space Agency)

Kim, J., Chevance, M., Kruijssen, J. M. D., et al. 2021a, MNRAS, 504, 487

Kim, J., Chevance, M., Kruijssen, J. M. D., et al. 2022, MNRAS, 516, 3006

Kim, J., Chevance, M., Kruijssen, J. M. D., et al. 2023, ApJL, 944, L20

Kim, J.-G., Ostriker, E. C., & Filippova, N. 2021b, ApJ, 911, 128

Kleinmann, D. E., & Low, F. J. 1967, ApJL, 149, L1

Kourkchi, E., Courtois, H. M., Graziani, R., et al. 2020, AJ, 159, 67

Kourkchi, E., & Tully, R. B. 2017, ApJ, 843, 16

Kreckel, K., Faesi, C., Kruijssen, J. M. D., et al. 2018, ApJL, 863, L21

Kretschmer, M., & Teyssier, R. 2020, MNRAS, 492, 1385

Kruijssen, J. M. D. 2012, MNRAS, 426, 3008

Kruijssen, J. M. D., & Longmore, S. N. 2014, MNRAS, 439, 3239

Kruijssen, J. M. D., Schruba, A., Hygate, A. P. S., et al. 2018, MNRAS, 479, 1866

Kruijssen, J. M. D., Schruba, A., Chevance, M., et al. 2019a, Natur, 569, 519

Kruijssen, J. M. D., Dale, J. E., Longmore, S. N., et al. 2019b, MNRAS, 484, 5734

Krumholz, M. R. 2014, PhR, 539, 49

Krumholz, M. R., & McKee, C. F. 2005, ApJ, 630, 250

Krumholz, M. R., & McKee, C. F. 2020, MNRAS, 494, 624

Krumholz, M. R., McKee, C. F., & Bland-Hawthorn, J. 2019, ARA&A, 57, 227

Krumholz, M. R., & Tan, J. C. 2007, ApJ, 654, 304

Lang, P., Meidt, S. E., Rosolowsky, E., et al. 2020, ApJ, 897, 122

Larsen, S. S. 2009, A&A, 494, 539

Larson, K., Lee, J., Thilker, D., et al. 2022, arXiv:2212.11425

Lee, E. J., Miville-Deschenes, M.-A., & Murray, N. W. 2016, ApJ, 833, 229

Lee, J. C., Whitmore, B. C., Thilker, D. A., et al. 2022, ApJS, 258, 10

Leroy, A. K., Sandstrom, K., Rosolowsky, E., et al. 2023, ApJL, 944, L9

Leroy, A. K., Walter, F., Sandstrom, K., et al. 2013, AJ, 146, 19

Leroy, A. K., Schinnerer, E., Hughes, A., et al. 2017, ApJ, 846, 71

Leroy, A. K., Sandstrom, K. M., Lang, D., et al. 2019, ApJS, 244, 24

Leroy, A. K., Schinnerer, E., Hughes, A., et al. 2021, ApJS, 257, 43

Lindegren, L., Hernández, J., Bombrun, A., et al. 2018, A&A, 616, A2

Liu, D., Schinnerer, E., Cao, Y., et al. 2023, ApJL, 944, L19

Longmore, S. N., Kruijssen, J. M. D., Bastian, N., et al. 2014, in Protostars and Planets VI, ed. H. Beuther et al. (Tucson, AZ: Univ. of Arizona Press), 291

Lopez, L. A., Krumholz, M. R., Bolatto, A. D., et al. 2014, ApJ, 795, 121

Makarov, D., Prugniel, P., Terekhova, N., Courtois, H., & Vauglin, I. 2014, A&A, 570, A13

Meidt, S., Rosolowsky, E. W., Sun, J., et al. 2023, ApJL, 944, L18

Meidt, S. E., Hughes, A., Dobbs, C. L., et al. 2015, ApJ, 806, 72

Meidt, S. E., Leroy, A. K., Rosolowsky, E., et al. 2018, ApJ, 854, 100

Meidt, S. E., Glover, S. C. O., Kruijssen, J. M. D., et al. 2020, ApJ, 892, 73

Mooney, T. J., & Solomon, P. M. 1988, ApJL, 334, L51

Muñoz-Mateos, J. C., Sheth, K., Regan, M., et al. 2015, ApJS, 219, 3

Murray, N. 2011, ApJ, 729, 133

Nersesian, A., Xilouris, E. M., Bianchi, S., et al. 2019, A&A, 624, A80

Neugebauer, G., Habing, H. J., van Duinen, R., et al. 1984, ApJL, 278, L1

Nugent, P., Sullivan, M., Ellis, R., et al. 2006, ApJ, 645, 841

Oey, M. S., & Clarke, C. J. 1997, MNRAS, 289, 570

Olivier, G. M., Lopez, L. A., Rosen, A. L., et al. 2021, ApJ, 908, 68

Onodera, S., Kuno, N., Tosaki, T., et al. 2010, ApJL, 722, L127

Padoan, P., Haugbølle, T., Nordlund, Å., & Frimann, S. 2017, ApJ, 840, 48
Pan, H.-A., Schinnerer, E., Hughes, A., et al. 2022, ApJ, 927, 9
Perrin, M. D., Sivaramakrishnan, A., Lajoie, C.-P., et al. 2010, Proc. SPIE, 9143, 91433X
Pilbratt, G. L., Riedinger, J. R., Passvogel, T., et al. 2010, A&A, 518, L1
Pilyugin, L. S., & Grebel, E. K. 2016, MNRAS, 457, 3678
Portegies Zwart, S. F., McMillan, S. L. W., & Gieles, M. 2010, ARA&A, 48, 431
Riechers, D. A., Pope, A., Daddi, E., et al. 2014, ApJ, 786, 31
Rodriguez, J., Lee, J., Whitmore, B., et al. 2023, ApJL, 944, L26
Rosolowsky, E., Hughes, A., Leroy, A. K., et al. 2021, MNRAS, 502, 1218
Ryon, J. E., Gallagher, J. S., Smith, L. J., et al. 2017, ApJ, 841, 92
Saintonge, A., Catinella, B., Tacconi, L. J., et al. 2017, ApJS, 233, 22
Salim, S., Boquien, M., & Lee, J. C. 2018, ApJ, 859, 11
Salim, S., Rich, R. M., Charlot, S., et al. 2007, ApJS, 173, 267
Salim, S., Lee, J. C., Janowiecki, S., et al. 2016, ApJS, 227, 2
Sandstrom, K., Chastenet, J., Sutter, J., et al. 2023a, ApJL, 944, L7
Sandstrom, K. M., Koch, E. W., Leroy, A. K., et al. 2023b, ApJL, 944, L8
Santoro, F., Kreckel, K., Belfiore, F., et al. 2022, A&A, 658, A188
Scheuermann, F., Kreckel, K., Anand, G. S., et al. 2022, MNRAS, 511, 6087
Schinnerer, E., Leroy, A., Blanc, G., et al. 2019a, Msngr, 177, 36
Schinnerer, E., Hughes, A., Leroy, A., et al. 2019b, ApJ, 887, 49
Schinnerer, E., Emsellem, E., Henshaw, J., et al. 2023, ApJL, 944, L15
Schlawin, E., Leisenring, J., Misselt, K., et al. 2020, AJ, 160, 231
Schruba, A., Kruijssen, J. M. D., & Leroy, A. K. 2019, ApJ, 883, 2
Schruba, A., Leroy, A. K., Walter, F., Sandstrom, K., & Rosolowsky, E. 2010, ApJ, 722, 1699
Semenov, V. A., Kravtsov, A. V., & Gnedin, N. Y. 2017, ApJ, 845, 133
Shaya, E. J., Tully, R. B., Hoffman, Y., & Pomarede, D. 2017, ApJ, 850, 207
Smith, J. D. T., Draine, B. T., Dale, D. A., et al. 2007, ApJ, 656, 770
Smithsonian Astrophysical Observatory 2000, Astrophysics Source Code Library, record ascl:0003.002
Soifer, B. T., Helou, G., & Werner, M. 2008, ARA&A, 46, 201
Soifer, B. T., Houck, J. R., & Neugebauer, G. 1987, ARA&A, 25, 187
Sun, J., Leroy, A. K., Schruba, A., et al. 2018, ApJ, 860, 172
Sun, J., Leroy, A. K., Schinnerer, E., et al. 2020, ApJL, 901, L8
Sun, J., Leroy, A. K., Rosolowsky, E., et al. 2022, AJ, 164, 43
Thilker, D., Lee, J. C., Deger, S., et al. 2023, ApJL, 944, L13
Thilker, D. A., Whitmore, B. C., Lee, J. C., et al. 2022, MNRAS, 509, 4094
Tielens, A. G. G. M. 2008, ARA&A, 46, 289
Turner, J. A., Dale, D. A., Lee, J. C., et al. 2021, MNRAS, 502, 1366
Utomo, D., Sun, J., Leroy, A. K., et al. 2018, ApJL, 861, L18
Ward, J. L., Kruijssen, J. M. D., Chevance, M., Kim, J., & Longmore, S. N. 2022, MNRAS, 516, 4025
Watkins, E., Barnes, A., Henny, K. F., et al. 2023, ApJL, 944, L24
Weisz, D. R., Skillman, E. D., Cannon, J. M., et al. 2009, ApJ, 704, 1538
Werner, M. W., Roellig, T. L., Low, F. J., et al. 2004, ApJS, 154, 1
Whitcomb, C. M., Sandstrom, K., Murphy, E. J., & Linden, S. 2020, ApJ, 901, 47
Whitmore, B., Chandar, R., Lee, J. C., et al. 2023a, MNRAS, 520, 63
Whitmore, B., Chandar, R., Rodriguez, J., et al. 2023b, ApJL, 944, L14
Whitmore, B. C., Lee, J. C., Chandar, R., et al. 2021, MNRAS, 506, 5294
Wild, V., & Hewett, P. C. 2005, MNRAS, 358, 1083
Williams, T., Sun, J., Barnes, A. T., et al. 2022, ApJL, 941, L27
Wright, E. L., Eisenhardt, P. R. M., Mainzer, A. K., et al. 2010, AJ, 140, 1868